INORGANIC CHEMISTRY
FRONTIERS

REVIEW

View Article Online
View Journal | View Issue

Cite this: *Inorg. Chem. Front.*, 2020, **7**, 817

Tungsten oxide-based visible light-driven photocatalysts: crystal and electronic structures and strategies for photocatalytic efficiency enhancement

Haiqin Quan, [a] Yanfeng Gao *[a] and Wenzhong Wang *[b]

Photocatalysis (PC) technology has received global attention due to its high potential of addressing both environmental and energy issues using only solar light as energy input. However, large-scale commercialization of PC technology is still far from expectation, which is primarily limited by low efficiency. The development of PC technology depends crucially on photocatalyst materials. In the past half century, TiO_2 has been mostly investigated and developed as a benchmark photocatalyst. However, TiO_2 responds intrinsically only to UV light, which has limited its efficient utilization of solar energy and restrained its applications to where UV light is not available, *e.g.*, indoor air purification. The development of novel intrinsically visible light-driven photocatalysts has been a new trend of PC technology. Amongst the various visible-light responsive candidates, tungsten oxides (WO_X, $X \leq 3$) have attracted much attention due to their diversely tunable stoichiometries and structures, suitable band gaps, chemical stability and Earth-abundance. However, bare WO_X exhibits comparatively low efficiency because of the fast recombination rate of photogenerated electrons and holes. Various strategies have been developed to enhance the photocatalytic efficiency of WO_X, including the controls in the crystal phase, stoichiometry/oxygen-vacancy, active facet and morphology, elemental doping, loading of noble metal nanoparticles, hybridization with carbon materials and coupling with other semiconductors to construct heterojunctions. This review summarizes firstly the fundamentals of WO_X (*i.e.*, crystal and electronic structures and optical properties) and then highlights the strategies for the enhancement of the photocatalytic efficiency of WO_X-based photocatalysts. The related synthesis methods are also briefly discussed. It is anticipated that this paper could offer a comprehensive understanding of WO_X-based photocatalysts and serve as a guideline for future designs of highly active visible light-driven WO_X-based photocatalysts.

Received 21st November 2019,
Accepted 26th December 2019

DOI: 10.1039/c9qi01516g

rsc.li/frontiers-inorganic

Introduction

In the past half century, photocatalysis (PC) technology has attracted global attention due to its high potential of addressing both environmental and energy issues using only solar light as energy input. To date, PC technology has been widely applied to various fields (see Fig. 1), such as water splitting for H_2 and O_2 generation,[1–6] CO_2 reduction for fuels and to alleviate the global warming crisis,[7,8] N_2 fixation for ammonia,[9] wastewater treatment,[10,11] air purification,[12,13] soil remediation,[14] self-cleaning surfaces,[15] anti-bacteria/virus,[16,17] *etc*. The merits of PC technology are fundamentally due to the strong

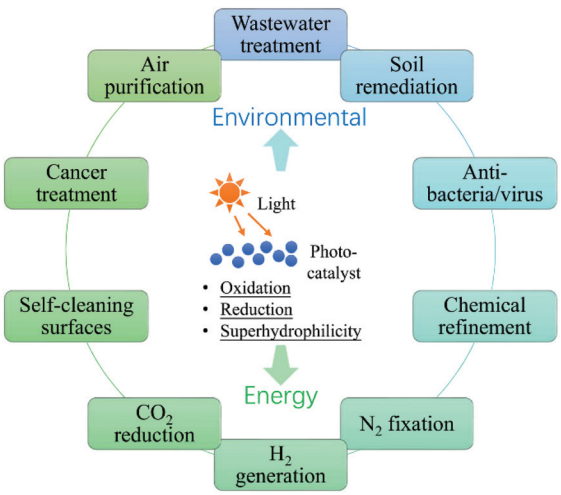

Fig. 1 Applications of photocatalysis.

[a]*School of Materials Science and Engineering, Shanghai University, Shanghai 200444, People's Republic of China. E-mail: yfgao@shu.edu.cn*
[b]*State Key Laboratory of High Performance Ceramics and Superfine Microstructure, Shanghai Institute of Ceramics, Chinese Academy of Science, Shanghai 200050, People's Republic of China. E-mail: wzwang@mail.sic.ac.cn*

redox ability of photocatalysts induced by proper illumination. However, large-scale commercialization of PC technology is still far from expectation, which is primarily limited by low efficiency.

The development of PC technology depends crucially on photocatalyst materials, which are generally semiconductors composed of a valence band (VB) filled with electrons and a conduction band (CB) empty of electrons. When irradiated by photons with energy higher than or equal to the band gap (*i.e.*, $h\nu \geq E_g$), a photocatalyst could be excited with part of electrons jumping from the VB to the CB, leaving excited electrons and holes in the CB and VB, respectively (see Fig. 2(i)).[18,19] The photogenerated electrons and holes, also called charge carriers, could transfer to the surface of the photocatalyst and then react with the adsorbed electron-acceptors (A) and electron-donors (D), respectively, initiating both photocatalytic reduction and oxidation reactions (Fig. 2(ii) and (iii)).[18,19] However, before participating in photocatalytic redox reactions, the photogenerated electron–hole pairs might have recombined quickly in bulk or on the surface of the photocatalyst (Fig. 2(iv) and (v)), as they are subjected to a strong Coulomb force.[20] This is one main reason for the low efficiency of photocatalysis.

In the past several decades, TiO_2 has been mostly investigated and developed as a benchmark photocatalyst.[21,22] However, as a wide band gap semiconductor (3.0–3.2 eV), TiO_2 responds intrinsically only to UV light that occupies merely 3–5% of the solar spectrum.[23] This has limited its efficient utilization of solar energy and restrained its applications to where UV light is not available, *e.g.*, indoor air purification. Although many efforts have been made to extend light absorption of TiO_2,[24–28] the efficiency of TiO_2-based photocatalysts under visible light irradiation is still unsatisfactory. In recent years, the development of novel intrinsically visible light-driven photocatalysts has been a new trend of PC technology. To date, various narrow bandgap (<3.0 eV) semiconductors have been developed as visible-light sensitive photocatalysts, such as WO_3,[29] α-Fe_2O_3,[30] CdS,[31] $BiVO_4$,[32] Bi_2WO_6,[33,34] Ag_3PO_4,[35] g-C_3N_4,[36] *etc*. Amongst them, tungsten oxides (WO_X, $X \leq 3$) have received increasing interest (a publication survey is shown in Fig. 3) due to their easy preparation, diversely tuneable stoichiometries and structures, suitable band gaps (2.4–2.8 eV, responsive to ~12% of the solar spectrum), strong photocatalytic oxidizing ability, high chemical stability, non-toxicity, and Earth-abundance.[37] Furthermore, WO_X possesses a much higher carrier mobility (10–12 $cm^2\ V^{-1}\ s^{-1}$) than TiO_2 (0.3 $cm^2\ V^{-1}\ s^{-1}$) and a comparatively longer hole diffusion length (150–500 nm) when compared with α-Fe_2O_3 (2–4 nm), both of which are essential for the transfer and separation of photogenerated charge carriers.[38,39] However, bare WO_X exhibits a relatively low efficiency because of the fast recombination rate of photogenerated charge carriers. This may have a close relationship with the low CB level (0.3–0.7 V *vs.* NHE) of WO_X that is not negative enough for the single-electron reduction of oxygen (*e.g.*, $O_2 + e^- = O_2^{\bullet-}$ (aq), −0.284 V; $O_2 + H^+ + e^- = HO_2^{\bullet}$ (aq), −0.046 V *vs.* NHE), which in turn, however, is important for the scavenging of photogenerated electrons.[40] As the photogenerated electrons could not be consumed efficiently, they accumulate and lead to the increased recombination rate of charge carriers.

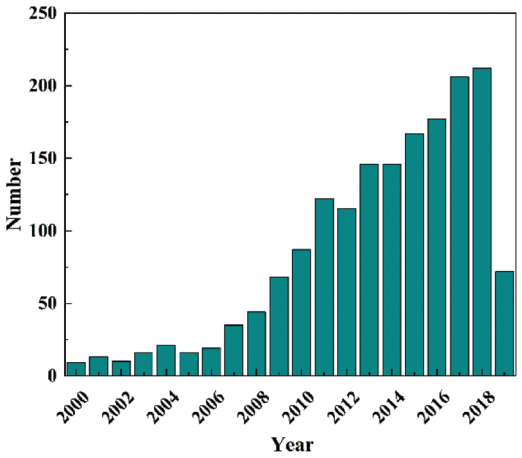

Fig. 3 Publication survey in Web of Science using "tungsten oxide" and "photocatalytic" as keywords (since 2000).

In the literature, many strategies have been developed to improve the photocatalytic behaviour of WO_X, such as the controls in the crystal phase,[41–43] stoichiometry/oxygen-vacancy,[38,44,45] active facet[46–48] and morphology,[49–51] elemental doping,[52–54] loading of noble metal nanoparticles (NPs),[55–57] hybridization with carbon materials[58–60] and coupling with other semiconductors to construct heterojunctions.[61–63] According to the basic PC processes (Fig. 2), any improvement in the following aspects can lead to an enhancement of the photocatalytic efficiency: (i) extend light absorption, (ii) facilitate charge transfer, (iii) inhibit the recombination of charge carriers, (iv) shorten the diffusion length for charge carriers, (v) increase the reactive sites on the surface of the photocatalyst, and (vi) increase the overall reaction surface area. The relationships between the various strategies and their possible resulted enhancements are summarized in Fig. 4.

Although there have been some review papers concerning WO_X-based photocatalysts, they paid attention to only limited

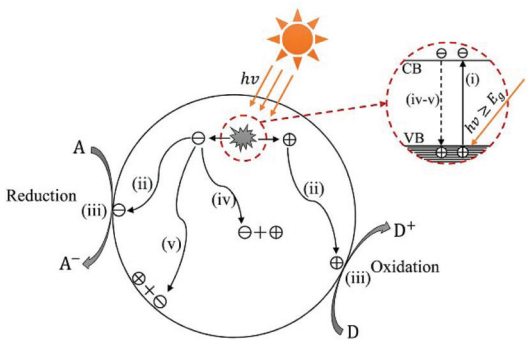

Fig. 2 Schematic photoexcitation in a solid photocatalyst followed by deexcitation (A: electron-acceptor; D: electron-donor).

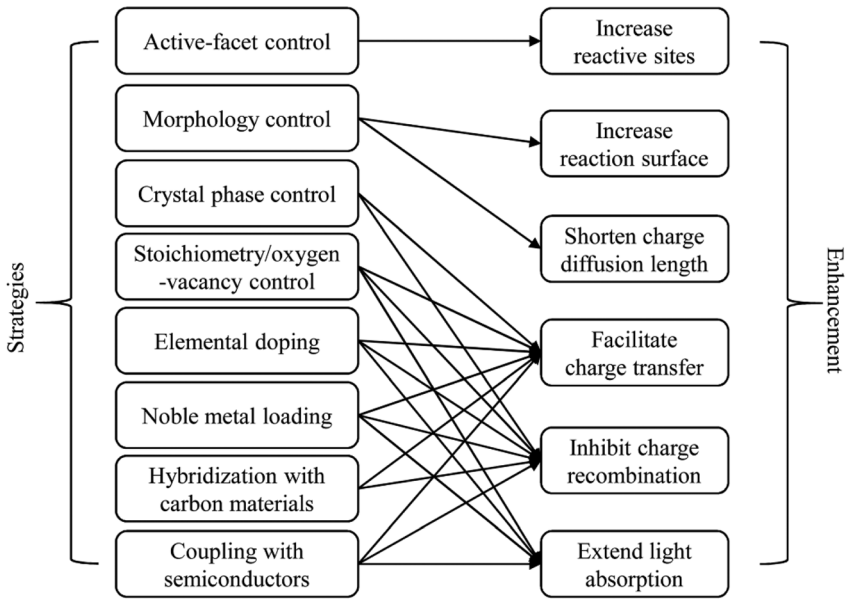

Fig. 4 Relationship between the strategies and their main possible resulted enhancements.

aspects, *e.g.*, nanostructured WO_3 thin films for photoelectrocatalytic (PEC) water oxidation[64] and nanostructured-based WO_3 for wastewater treatment.[65] A comprehensive review regarding WO_X-based photocatalysts, especially involving the advancements in the past few years, is still in need. This review summarizes firstly the fundamentals of WO_X (*i.e.*, crystal and electronic structures and optical properties) and then highlights the strategies for the improvement of the photocatalytic efficiency of WO_X-based photocatalysts. It is anticipated that this paper could serve as a guideline for future designs of highly active visible light-driven WO_X-based photocatalysts.

Fundamentals

Tungsten oxide (WO_X) is a big family that is composed of stoichiometric WO_3 and various sub-stoichiometric tungsten oxides (WO_{3-x}, $0 < x \leq 1$). As tungsten oxide hydrates ($WO_X{\cdot}nH_2O$) have a close relationship with their dehydrated counterparts and exhibit photocatalytic activity, they are considered herein as part of WO_X-based photocatalysts. In this section, the crystal and electronic structures and optical properties of WO_X and their hydrates are discussed.

Crystal structures

The ideal crystal structure of WO_3 is identical to the cubic ReO_3 type or ABO_3 perovskite structure in the absence of an A cation, *i.e.*, a three-dimensional network formed by corner-sharing WO_6 octahedra.[66] As illustrated in Fig. 5(a), the ideal cubic WO_3 has W atoms at the corners of a cube, each surrounded by six octahedrally coordinated oxygens; four oxygens lie in a plane containing the W atoms and there is one oxygen above and one below this plane for each W atom; each oxygen is common to two octahedra, giving the formula of WO_3. Cubic cavities with constant edges (about 2.7 Å, the length of O–O bonds) form the interstices of the network of WO_6 octahedra (regular four-membered rings can be seen in the [100], [010] and [001] directions, respectively, as shown in Fig. 5(c)). The ideal cubic WO_3 has never been observed experimentally.[67] Bulk WO_3 undergoes at least five reversible phase transitions upon heating or cooling (Fig. 6).[68–71] This involves the tetragonal (t- or α-WO_3),[70,72] orthorhombic (o- or β-WO_3),[73] monoclinic I (m- or γ-WO_3),[71] triclinic (tr- or δ-WO_3),[68] and monoclinic II (ε-WO_3) phases.[66] All these phases of WO_3 have a similar crystal structure to the ideal cubic WO_3, however, with a lowered symmetry owing to three possible types of distortions: displacement of the W atom from its octahedron and distortion and tilting of WO_6 octahedra.[66] According to Corà *et al.*, the lowering of the symmetry, especially by the off-central displacement of W atoms, results in an increase in the covalence between tungsten and its nearest oxygen, which thus leads to a more stable structure.[67] At room temperature, m-WO_3 has been reported as the most stable phase, with tr-WO_3 also being observed.[74] A hexagonal phase of WO_3 is also frequently reported,[75–77] which was firstly obtained by the dehydration of $WO_3{\cdot}0.33H_2O$ in 1979.[78] The hexagonal h-WO_3 is also build up from corner-sharing WO_6 octahedra but their arrangement results in three- and six-membered rings in the *ab*-planes and leads to the formation of large hexagonal tunnels (~5.6 Å) in the *c*-axis (see Fig. 5(c)). In the *ac*- and *bc*-planes, four-membered rings formed by WO_6 octahedra, as in other phases, are also the case in h-WO_3. According to Gerand *et al.*, the unit cell of h-WO_3 contains six molecules and shows lattice constants of a = 7.298 Å and c = 7.798 Å (Fig. 5(b)).[78] More information about the crystal structures and lattice parameters of polymorphic WO_3 can be found in Fig. 5(b) and (c).

(a)

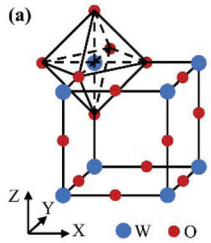

(b)

Cubic	Hexagonal	Tetragonal	Orthorhombic	Monoclinic I	Triclinic
Pm3m [221]	P6/mmm [191]	P4/ncc [130]	Pbcn [60]	$P2_1/b$ [14]	$P\bar{1}$ [2]
Z=1	Z=6	Z=4	Z=8	Z=8	Z=8
a=3.84 Å	a=7.298 Å	a=5.289 Å	a=7.333 Å	a=7.30 Å	a=7.309 Å
b=3.84 Å	b=7.298 Å	b=5.289 Å	b=7.573 Å	b=7.53 Å	b=7.522 Å
c=3.84 Å	c=7.798 Å	c=7.863 Å	c=7.740 Å	c=7.68 Å	c=7.678 Å
α=90°	α=90°	α=90°	α=90°	α=90°	α=88.81°
β=90°	β=90°	β=90°	β=90°	β=90.54°	β=90.92°
γ=90°	γ=120°	γ=90°	γ=90°	γ=90°	γ=90.93°

(c)

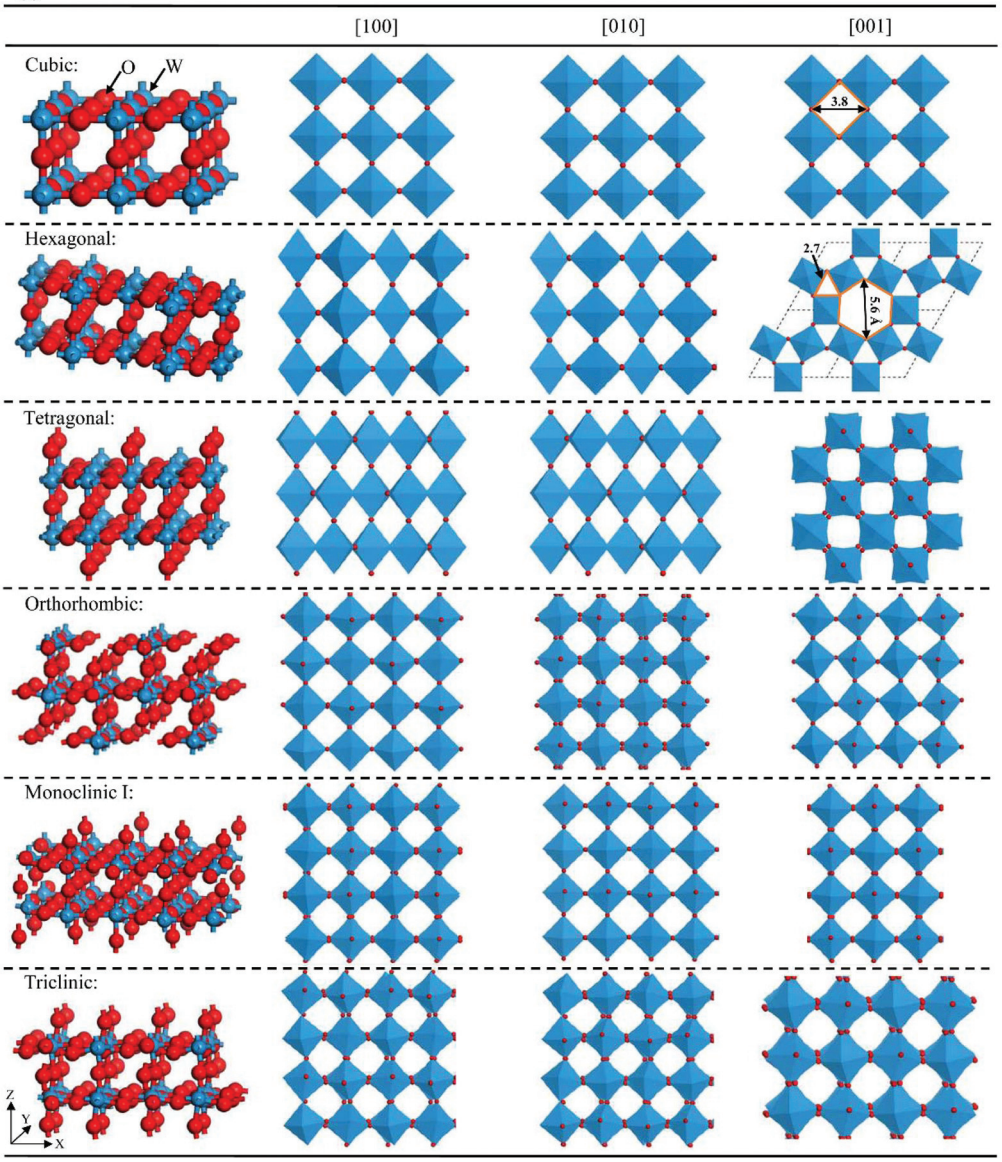

Fig. 5 Crystal structures of polymorphic WO_3: cubic WO_3 and its WO_6 octahedron (a), structural parameters (b), and stick–ball and polyhedral representations (c).

The lattice of WO_3 can sustain considerable amounts of oxygen vacancies, however, this is accompanied by structural changes according to the degree of reduction. In a sub-stoichiometric WO_{3-x} with a low degree of reduction ($x < 0.01$), single oxygen vacancies can be dispersed in the lattice in low concentration. However, with increasing x the lattice tends to eliminate single oxygen vacancies by a crystal shear (CS) mechanism, resulting in groups of edge-sharing WO_6 octahedra arranged along some crystallographic planes (shear planes, SPs). For moderate x, these SPs are isolated and can be regarded as extended defects.[79] With further increase in x, the SPs begin to interact and tend to align in parallel. If the SPs

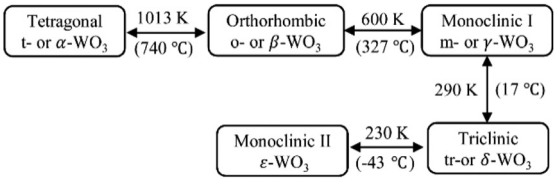

Fig. 6 Classical phase transitions of bulk WO_3 upon heating or cooling.[68–71]

are all in parallel and equidistant, a crystal phase with a defined structure arises, which can be recognized as the Magnéli W_nO_{3n-2} series.[80] One such typical example is $W_{20}O_{58}$ ($WO_{2.9}$), the structure of which is demonstrated in Fig. 7(a). When $x \geq 0.13$, structures with pentagonal columns (PCs) become dominant. These structures contain two kinds of coordination polyhedra, *viz.*, WO_6 octahedra and WO_7 pentagonal bipyramids. The WO_7 bipyramids share their equatorial edges with five WO_6 octahedra to form groups of PCs (generally parallel to the monoclinic *b*-axis). The variations of such structures depend on the modes of the linking of the PCs.[81] One such typical example is $W_{18}O_{49}$ ($WO_{2.72}$), as shown in Fig. 7(b). Other frequently investigated WO_{3-x} with defined structures, also known as the Magnéli phases, include $W_{32}O_{84}$ ($WO_{2.625}$), W_3O_8 ($WO_{2.67}$), $W_{17}O_{47}$ ($WO_{2.76}$), W_5O_{14} ($WO_{2.8}$), $W_{25}O_{73}$ ($WO_{2.92}$), *etc.*[82]

Hydrated tungsten oxides $WO_X{\cdot}nH_2O$ have been frequently obtained as intermediate products during the synthesis of WO_X using a wet chemical route before annealing. The most widely investigated $WO_X{\cdot}nH_2O$ photocatalysts include monoclinic $WO_3{\cdot}2H_2O$ (dihydrate),[83] orthorhombic $WO_3{\cdot}H_2O$ (monohydrate),[84,85] cubic pyrochlore-type $WO_3{\cdot}0.5H_2O$ (hemihydrate),[86] and orthorhombic $WO_3{\cdot}0.33H_2O$.[87] The crystal structures of $WO_3{\cdot}nH_2O$ are highly dependent on their water content. $WO_3{\cdot}2H_2O$ is built up from layers of corner-sharing $WO_5(OH_2)$ octahedra and interlayer water molecules (Fig. 8(a)).[88] Each $WO_5(OH_2)$ octahedron consists of one W atom at the centre, one terminal oxygen, one coordinated water and four bridging oxygens, with which $WO_5(OH_2)$ octahedra are connected to each other in the *ac*-planes forming neutral $WO_3{\cdot}H_2O$ layers. The interlayer water molecules connect with $WO_5(OH_2)$ octahedra through hydrogen bonds.[88] $WO_3{\cdot}H_2O$ can be obtained by removing the interlayer water from $WO_3{\cdot}2H_2O$ (Fig. 8(b)).[89,90] $WO_3{\cdot}0.5H_2O$ is less documented and believed to have a structure of cubic pyrochlore-type, where the water molecules are presented in tunnels along the [110] direction, constructed by six-membered rings of corner-sharing WO_6 octahedra (Fig. 8(c)).[91] $WO_3{\cdot}0.33H_2O$ has been reported to consist of both WO_6 and $WO_5(OH_2)$ octahedra.[92] A typical representation of orthorhombic $WO_3{\cdot}0.33H_2O$ is demonstrated in Fig. 8(d), where three- and six-membered rings are formed by corner-sharing WO_6 and $WO_5(OH_2)$ octahedra in the *ab*-planes.[93]

Electronic band structures and optical properties

WO_3 is an n-type semiconductor with an indirect bandgap E_g characterizing the energy difference between the VB (E_{VB}) and the CB (E_{CV}), as shown in Fig. 9(a). The VB of WO_3 is formed by filled O 2p-orbitals while the CB is composed mainly of empty W 5d-orbitals.[94] The relationships between E_{VB}, E_{CB} and E_g follow the equations: (1) $E_{CB} = \chi - E^e - 0.5E_g$ and (2) $E_g = E_{VB} - E_{CB}$, where χ is Mulliken's electronegativity of the material (6.59 eV for WO_3) and E^e is the energy of a free electron on the hydrogen scale (4.5 eV).[85] This indicates that the positions of the VB and the CB for a specific material are influenced directly by the bandgap E_g. Bulk WO_3 has a typical E_g of 2.6 eV at room temperature, corresponding to a light absorption threshold at 477 nm determined by $\lambda = 1240/E_g$ and E_{VB} and E_{CB} at +3.39 eV and +0.79 eV, respectively.[95] This implies that the photogenerated holes in the VB of WO_3 is highly oxidizing, which is strong enough to decompose water ($E(O_2/H_2O)$ = +1.23 V *vs.* NHE) and almost all organic compounds, and/or react with water and surface hydroxyl (OH^-) to produce $^{\bullet}OH$ ($E(^{\bullet}OH/OH^-)$ = +1.99 V, $E(^{\bullet}OH/H_2O)$ = +2.72 V *vs.* NHE).[96] However, the photogenerated electrons in the CB of WO_3 are comparatively weak, which are not negative enough to photoreduce H^+ for H_2 ($E(H^+/H_2)$ = 0 V *vs.* NHE) and oxygen to $O_2^{\bullet-}$ ($E(O_2^{\bullet-}/O_2)$ = −0.284 V *vs.* NHE).[97] The E_g of WO_3 is obviously affected by the phase transitions, which in turn is a function of temperature. In general, E_g decreases and becomes increasingly diffuse as the temperature increases, indicating a redshift of the light absorption edge.[66] At the nanoscale, especially

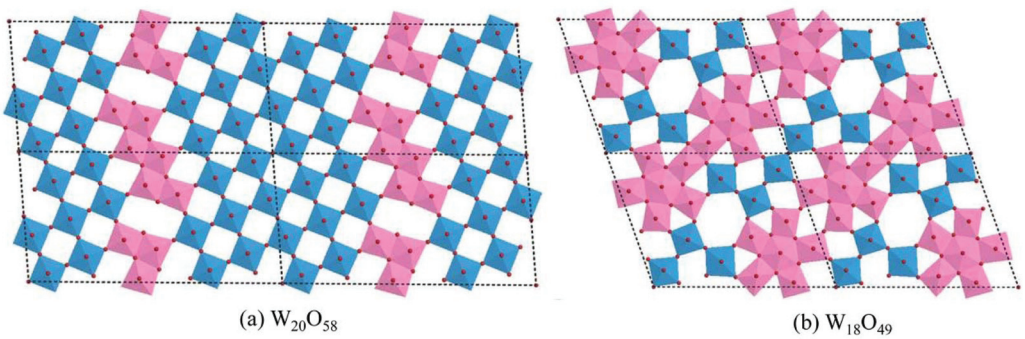

Fig. 7 Idealized structures of $W_{20}O_{58}$ (a) and $W_{18}O_{49}$ (b) looking down from the [010] direction.

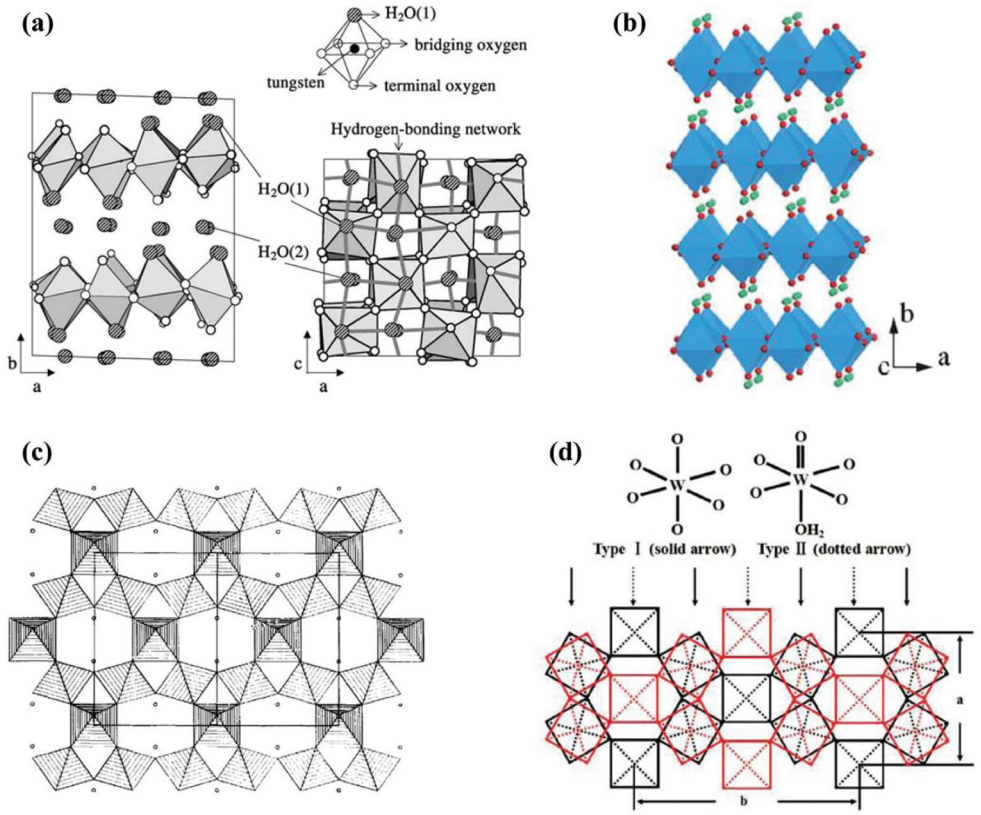

Fig. 8 Crystal structures of tungsten oxide hydrates: monoclinic $WO_3 \cdot 2H_2O$ (a),[88] orthorhombic $WO_3 \cdot H_2O$ (green balls represent H atoms) (b),[90] projection of cubic pyrochlore-type $WO_3 \cdot 0.5H_2O$ in the [110] direction (small circles represent water molecules) (c),[91] and orthorhombic $WO_3 \cdot 0.33H_2O$ (d).[93] Reprinted with permission from ref. 88, 90, 91 and 93. Copyright 2004 Elsevier, 2012 the Royal Society of Chemistry, 1989 Elsevier, and 2008 American Chemical Society, respectively.

when the particle size is close to or smaller than the exciton Bohr radius of the material (~3 nm for WO_3),[98] E_g might increase significantly with decreasing particle size owing to the quantum confinement (QC) effect.[99] The particle size effect on E_g can be estimated by Brus' equation,[100] as shown in Fig. 9(b).[101] It indicates that the E_g of WO_3 would be increased up to ~3.0 eV when the particle size is reduced to ~3 nm, implying that WO_3 quantum dots (QDs, sizes smaller than the exciton Bohr radius) need UV light for excitation. The E_{CB} of WO_3 QDs would be lifted upwards due to the expansion of the bandgap, resulting in enhanced photo-reducing ability. An experimental measurement of bandgap expansion and obviously uplifted E_{CB} of WO_3 QDs has been reported by Watanabe *et al.*, where the WO_3 QDs with sizes at the sub-nano scale show E_g values up to 3.7 eV and achieve single-electron reduction of molecular oxygen.[102]

Partial loss of oxygen from WO_3 has similar consequences to the insertion of donors.[103] Both experimental and simulation studies have revealed that the density of free charge carriers (N_D) in WO_{3-x} increases with the number of oxygen vacancies. As reported by Migas *et al.*, N_D increases from 2.90×10^{21} to 1.62×10^{22} cm^{-3} when the sub-stoichiometry is varied from $WO_{2.92}$ to $WO_{2.625}$.[82] The introduction of oxygen vacancies would lead to partial reduction of WO_3 ($W^{6+} \rightarrow W^{5+/4+}$) in order to match the charge balance. The presence of $W^{5+/4+}$ creates new states closely below the CB of WO_3 (W^{6+}), as shown in Fig. 9(c). The injected electrons by oxygen vacancies would be firstly trapped in the W 5d-orbitals in the $W^{5+/4+}$ sites, and then polarize the surrounding lattice to generate polarons.[104] WO_{3-x} has been reported to possibly absorb light ranging from the UV to near-infrared (NIR) regions due to three distinct modes of electron excitation: (i) VB-to-CB transition, (ii) VB-to-$W^{5+/4+}$ state transition, and (iii) polaron-induced localized surface plasmon resonance (LSPR) (Fig. 9(c)).[38] A typical light absorption of WO_{3-x} was demonstrated by Kalanur *et al.*, as shown in Fig. 9(d).[38] The strong absorption in the visible and NIR regions (above 500 nm) has been ascribed to the third mode of electron excitation, *i.e.*, the polaron-induced LSPR. The intensity of LSPR absorption has been proved to be correlated with N_D, where a large N_D generally leads to a strong LSPR absorption. Some recent reports also suggest that the oxygen deficiency results in the formation of oxygen-vacancy (V_O) states above and partly overlap with the VB.[105,106] This leads to an extension of the VB and narrows the band gap, which then expands the photo-response of WO_{3-x} toward the longer wavelength range.

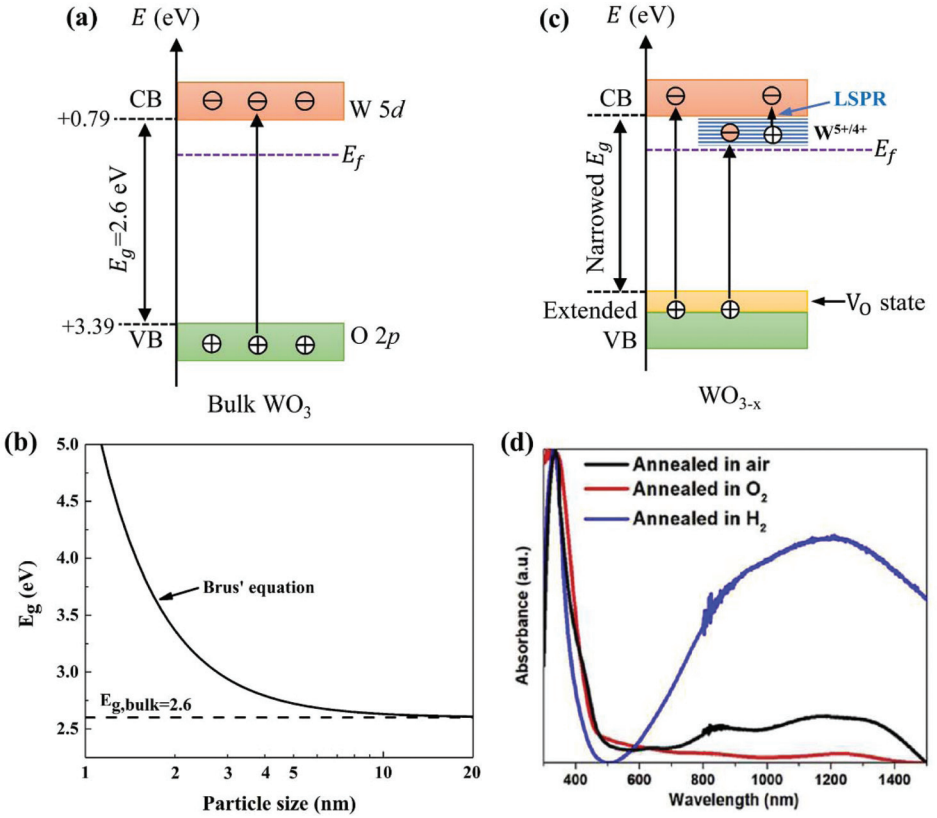

Fig. 9 Electronic band structure of stoichiometric bulk WO_3 (a), effect of the particle size on E_g for WO_3 predicted by Brus' equation with $m_e^* = 0.16m_0$ and $m_h^* = 0.53m_0$ (m_e^* and m_h^* are the effective mass of an electron and a hole, respectively; m_0 is the electron rest mass) (b),[101] electronic band structure and electron excitation modes in sub-stoichiometric WO_{3-x} (c), typical light absorptions of WO_X with different extents of oxygen vacancies (d).[38] Reprinted with permission from ref. 38. Copyright 2019 Elsevier.

As for $WO_X{\cdot}nH_2O$ photocatalysts, they generally show smaller E_g than their dehydrated counterparts due to the weaker binding energy, thus exhibiting larger light absorption ranges.[41,85] For instance, Ke *et al.* have synthesized $WO_3{\cdot}H_2O$ *via* a hydrothermal process and then obtained WO_3 by calcining the as-synthesized sample at 500 °C.[85] Their $WO_3{\cdot}H_2O$ and WO_3 samples exhibit light absorption edges at 530 nm (E_g = 2.44 eV) and 472 nm (E_g = 2.64 eV), respectively.

Enhancement strategies

In order to improve the photocatalytic behaviours of WO_X, many enhancement strategies have been reported. In this section, various enhancement strategies will be summarized from the aspects of the controls in the crystal phase, stoichiometry/oxygen-vacancy, active facet and morphology, elemental doping, loading of noble metal NPs, hybridization with carbon materials and coupling with other semiconductors to construct heterojunctions.

Phase control

Apart from m-WO_3, nanostructured WO_3 in hexagonal,[42,48] orthorhombic[107,108] and triclinic phases[109,110] have also been reported to retain phase stability and exhibit photocatalytic activity at room temperature. Although some studies have reported that m-WO_3 exhibits better photocatalytic behaviours than other phases of WO_3,[42,107] it is still difficult to make a conclusive comparison, for the photocatalytic efficiency of WO_X is influenced simultaneously by many factors.

Recently, a phase junction photocatalyst constructed by different phases of the same semiconductor has attracted much attention due to its simplicity, controllability and great photocatalytic activity. WO_X is a polymorphic semiconductor that consists of many crystal phases and abundant hydrates, which has offered great possibility to construct phase junctions between different phases. Some WO_X-based phase junction photocatalysts have been reported, such as h-$WO_3{\cdot}0.33H_2O$/c-$WO_3{\cdot}0.5H_2O$,[43] h-WO_3/m-WO_3 [111] and o-$WO_3{\cdot}0.33H_2O$/h-WO_3.[41] The enhancement mechanism depending on the phase junction is mainly due to the improved electron–hole separation between the different phases which show unequal band structures. A typical phase junction photocatalyst with the corresponding charge transfer mechanism is demonstrated in Fig. 10.

In general, a phase junction could be obtained by applying the intermediate synthesis conditions located between those for the synthesis of single-phase tungsten oxides. The mass

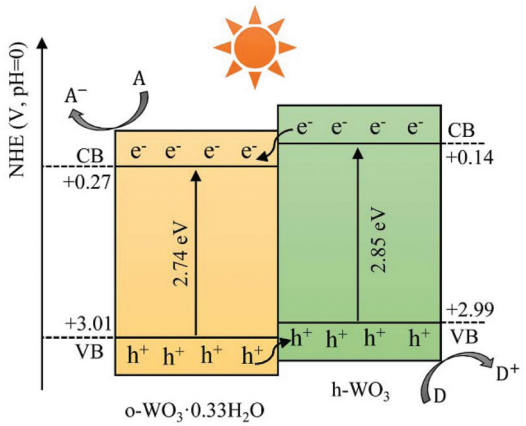

Fig. 10 Schematic illustration of charge transfer and separation in a typical phase junction constructed by o-WO_3·0.33H_2O and h-WO_3.

ratio between the combined phases can be tuned by shifting the conditions toward the synthesis of the phase that is expected to increase. For instance, Li *et al.* have prepared a phase junction photocatalyst of o-WO_3·0.33H_2O/h-WO_3 *via* a hydrothermal method by adjusting the amount of NaCl (a capping agent).[41] They obtained pure o-WO_3·0.33H_2O in the absence of NaCl and pure h-WO_3 with the addition of 0.4 g NaCl. Their phase junction was obtained when NaCl was applied between 0.1 and 0.2 g and the mass ratio of o-WO_3·0.33H_2O to h-WO_3 decreases when the amount of NaCl increases.

Stoichiometry/oxygen-vacancy control

In recent years, many efforts have been made to improve the photocatalytic efficiency of WO_X by tuning its oxygen vacancies (*e.g.*, number and distribution). Many studies have confirmed that the photocatalytic efficiency of WO_{3-x} increases as the number of oxygen vacancies increases, due to enhanced optical absorption and reduced recombination rate of charge carriers. However, an over-abundance of oxygen vacancies (*i.e.*, more than the optimal level) can act as recombination or trap centres for the photogenerated electrons and holes, thus lowering the photocatalytic activity.[38,45] Some studies suggest that the distribution of oxygen vacancies (*i.e.*, in bulk or on the surface) also matters to the photocatalytic activity, however, in different ways.[44,45,112,113] Wang *et al.* have reported that bulk oxygen vacancies mainly promote visible light harvesting and slightly restrain the recombination of electrons and holes by narrowing the band gap, while the surface oxygen vacancies significantly increase the charge separation efficiency by lowering the VB edge.[45]

Oxygen vacancies in WO_3 can be introduced by several means, including annealing under oxygen-deficient atmospheres (*e.g.*, hydrogen[45] and vacuum[114]), hydrogen peroxide treatment,[112] etching and by specific routes.[39,98,115] By annealing, which is the most common way, the extent and distribution of oxygen vacancies can be tuned by varying the temperature, duration and atmosphere. In general, the extent of oxygen vacancies increases as the reducibility of the atmosphere and the thermal treatment time increase. A moderate reductive atmosphere (*e.g.*, 20% H_2 in N_2) is generally beneficial for generating surface oxygen vacancies, while thermal treatment under a highly reductive atmosphere (*e.g.*, 100% H_2) favours the generation of bulk oxygen vacancies. Oxygen vacancies generally propagate from the surface into the bulk as the thermal treatment proceeds. The oxygen vacancies can also be introduced by annealing in air, because, depending on the crystal structure and annealing temperature, the critical phase transition and nanoscale inhomogeneous deformation (during annealing) in the WO_3 lattice can also create oxygen vacancies.[105]

Amongst the various oxygen-deficient tungsten oxides, $W_{18}O_{49}$ has attracted much attention due to its stable defect structure, strong LSPR absorption and good photocatalytic performance.[116–118] $W_{18}O_{49}$ nanowires preferentially growing along the [010] direction have been frequently reported and applied to various photocatalytic reactions (*e.g.*, CO_2 reduction to CH_4,[119] degradation of organic dyes[120] and H_2 generation[114]). They have been synthesized by various methods, such as a solvothermal reaction followed by vacuum drying[119] and solution combustion synthesis.[120]

Active-facet control

As photocatalytic reactions occur on the surface of the photocatalyst, the surface features (*e.g.*, energy, atomic coordination and electronic structure) influence directly the overall photocatalytic reactivity. It has been widely accepted that high surface energy results in high photocatalytic reactivity due to the more active sites and stronger adsorption ability. From this point of view, {002} is the most active facet for both m- and o-WO_3, for their surface energies follow the order: {002} (1.56 J m^{-2}) > {020} (1.54 J m^{-2}) > {200} (1.43 J m^{-2})[121] and {002} (1.74 J m^{-2}) > {020} = {200} (1.69 J m^{-2}),[122] respectively. This has been confirmed by several experimental measurements where both m- and o-WO_3 with the preferentially exposed {002} facets exhibit better photocatalytic performance than their counterparts without the preferred orientation of the crystal facets.[46,50,123,124] The properties of exposed facets have a close relationship with the crystal phase which they belong to. For h-WO_3, both {002} and {200} have been reported to be active facets, the photocatalytic enhancement of which was ascribed to the increased charge separation efficiency.[48,125] For o-WO_3·0.33H_2O, however, {020} was reported to be the most active facet, which has been said to be correlated with the unique W=O and O–H groups.[47]

Some studies suggest that the exposed facets have influences on the electronic structure, thus affecting the reduction and oxidation abilities of the photocatalyst. Xie *et al.* have prepared a quasi-cubic-like WO_3 crystal with a nearly equal percentage of the {002}, {020} and {200} facets and a rectangular sheet-like WO_3 crystal with the predominant {002} facet. Their study demonstrates that the former exhibits a deeper VB maximum, thus showing a much higher O_2 evolution rate in photocatalytic water oxidation, while the latter exhibits an elev-

ated CB minimum, and thus is able to photo-reduce CO_2 to CH_4.[121]

Hydrothermal/solvothermal synthesis has been commonly used to control the exposed facets of WO_X. It is well established that solvents, impurities and additives in solution can substantially influence the ultimate shape of the crystals by controlling their growth rate in specific directions. For instance, Liang *et al.* have synthesized 2D ultra-thin m-WO_3 nanosheets with more than 90% of the exposed {002} crystal facets *via* using a surfactant (Pluronic P123) as a capping agent.[50] Since the surface energy of the {002} facet is much higher than that of the {020} and {200} facets, the polar groups of P123 preferentially adsorb onto the {002} facets, thus inhibiting their growth and finally promoting their exposure. Some inorganic salt anions, such as NO_3^-,[121] BF_4^-,[122] Cl^- (ref. 46) and SO_4^{2-},[48] have also been reported as effective capping agents for the preferential exposure of the {002} facets for m- and o-WO_3 due to their preferential adsorption onto the {002} facets.

Morphology control

Morphology, mainly characterizing the features of shape and size, is one of the most important factors influencing the performance of photocatalysts. In general, a morphology that could offer a large specific surface area, large number of active sites, suitable pore features and short diffusion length for charge carriers is desirable.

Various unique morphologies of WO_X photocatalysts have been reported in the literature; a brief summary can be found in Fig. 11. These morphologies can be classified into zero-dimensional (0D, *e.g.*, spherical and pseudo-spherical NPs[102,126–128]), one-dimensional (1D, *e.g.*, nanorods,[120] nanowires,[114] nanobelts,[129] nanofibers[130,131] and nanotubes[23]), two-dimensional (2D, *e.g.*, nanoplatelets,[132] nanoplates[48] and nanosheets[133]) and three-dimensional (3D, *e.g.*, porous interconnected structures,[134,135] core–shell structures[136–139] and hierarchical structures assembled by low-dimensional building blocks[46,51,140–144]) according to the dimensionality. A schematic illustration of simplified structures in different dimensionalities is demonstrated in Fig. 12(a). With a specific volume, particles in different shapes show different specific surface areas. A comparison of the specific surface area (*S*) between nanospheres, nanorods and nanosheets with different aspect ratios is demonstrated in Fig. 12(b). It indicates that, for both 1D nanorods and 2D nanosheets, the specific surface area increases as the aspect ratio increases. The 0D nanosphere shows the smallest specific surface area. It can be concluded that, if only considering the specific surface area, the preferability of morphology follows the order: 2D (high aspect ratio) > 1D (high aspect ratio) > 0D. However, it should always be kept in mind that a large specific surface area tends to result in severe agglomeration due to high specific surface energy, which in turn is not beneficial for the photocatalytic performance. Compromised strategies might be considered when developing efficient photocatalysts for practical applications. Apart from the shape, the size matters as well. In general, a smaller size results in a larger specific surface area and a shorter diffusion length for charge transfer, both of which are desirable for the enhancement of photocatalytic efficiency. When the particle size (at least in one dimension) is reduced to be close to or smaller than the exciton Bohr radius (~3 nm for WO_3), the band gap of the material would be increased significantly with the CB edge uplifted due to the strong QC effect.

The morphology of WO_X can be controlled by using a template-based method or a template-free method. With a template method, the shape and size of WO_X are determined primarily by the structure of the template. Two such typical examples are WO_3 QDs in macro/mesoporous silica[102,126] and 3D ordered macroporous WO_3.[134,135] In a typical synthesis process, a precursor solution is simply introduced into template pores followed by particulation or chemical reactions for conversion to WO_X. The template can be removed by using specific routes depending on the template material (*e.g.*, calcination for removing the polymer template[145]) or just kept as a support for the WO_X catalyst.[102] With a template-free method, the shape and size of WO_X can be tuned by varying the synthesis conditions (*e.g.*, type and concentration of the capping agent, pH, and reaction temperature and time), which are influencing factors for the nucleation and growth rate of crystals in specific directions. For instance, Shukla *et al.* have synthesized monodisperse spherical WO_3 NPs using cationic surfactants (*i.e.*, cetylpyridinium chloride (CPyC), cetylpyridinium bromide (CPyB), hexadecyltrimethyl ammonium bromide (HTAC) and tetradecyltrimethyl ammonium bromide (TTAB)) as a capping agent.[128] As these cationic surfactants adsorb non-selectively onto the surface of the WO_3 nuclei, the final product of WO_3 is in a spherical shape. When agents that can selectively adsorb onto specific faces of WO_3 are applied, 1D and/or 2D structures might be obtained.

Elemental doping

Elemental doping is an effective way to tune the properties of photocatalysts. The incorporation of foreign ions into the lattice of WO_X may result in changes in the crystal structure, morphology, electronic structure and optical properties depending on the nature and concentration of the dopant and the doping routes. The incorporated ions have two possible positions in the lattice of WO_X, *i.e.*, the W or O sites (substitution) and the interstice between WO_6 octahedra (intercalation). The feasibility and extent of doping depend crucially on the differences in the radius and valence state between the dopant and host atoms. In general, a dopant with a similar radius to that of the host atom is easier for achieving doping and has a higher solubility in the host lattice, and simultaneously, resulting in lighter distortions of the host lattice and smaller changes in the morphology. Compared to anion doping (*e.g.*, I^- doping[52]), cation doping with low valence metal ions is much more frequently reported, such as Mo^{5+},[146,147] Ta^{5+},[148] Nb^{5+},[149] Ti^{4+},[150] Sn^{4+},[151] Bi^{3+},[152] Fe^{3+},[153,154] Yb^{3+},[155] Ce^{3+},[156] La^{3+},[156] Y^{3+},[156] Co^{2+},[157] Cu^{2+},[158] Zn^{2+},[159] Ni^{2+},[160] *etc*. In order to maintain the charge balance, oxygen

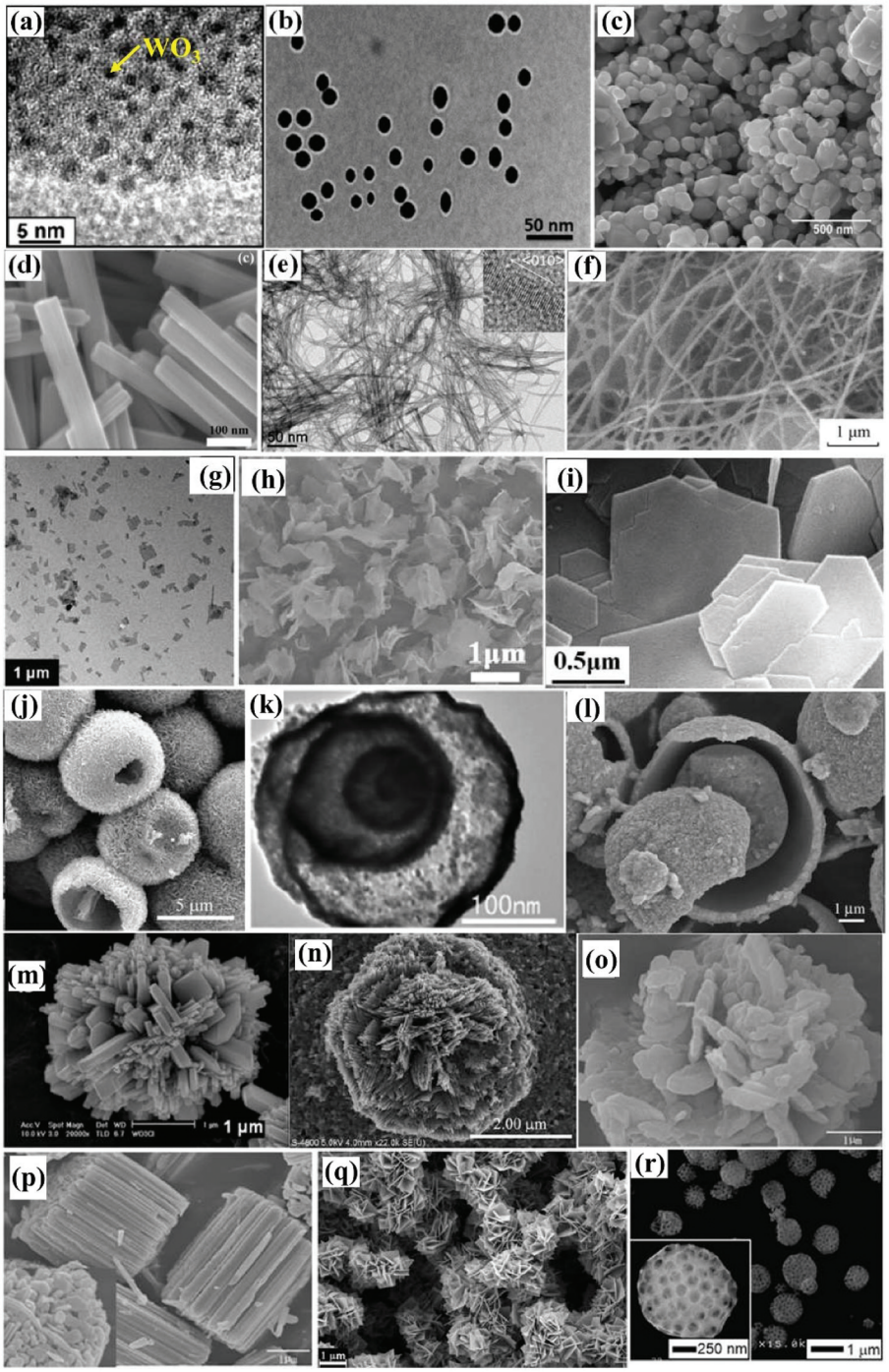

Fig. 11 Typical morphologies of WO_X photocatalysts from the literature: QDs (a),[126] monodisperse nanoparticles (b),[128] aggregated nanoparticles (c),[42] nanorods (d),[77] nanowires (e),[98] nanofibers (f),[131] nanosheets (g),[133] nanosheets (h),[50] nanoplates (i),[48] hollow microspheres (j),[137] multiple-shell hollow spheres (k),[139] sphere-in-shell microstructures (l),[138] hierarchical structures (m),[141] flower-like microstructures (n),[142] flower-like microstructures (o),[143] cylindrical-stack microstructures (p),[143] hierarchical structures (q),[144] and 3D ordered macroporous structures (r).[135] Reproduced with permission from ref. 42, 48, 50, 77, 98, 126, 128, 131, 133, 135, 137–139 and 141–144. Copyright 2010 the Royal Society of Chemistry, 2016, 2014 and 2017 Elsevier, 2018 American Chemical Society, 2015 Springer Nature, 2012 American Chemical Society, 2019, 2017 and 2008 Elsevier, 2012 and 2008 John Wiley and Sons, 2013, 2009, 2014, 2018 and 2013 Elsevier, respectively.

vacancies are generally created when low valence metal ions are doped, which could result in extra benefit for the improvement of the photocatalytic performance. The doped metal ions on the surface of WO_X could trap and localize electrons around them and enhance the photo-induced electron density on the active sites, so as to improve the electron-giving ability

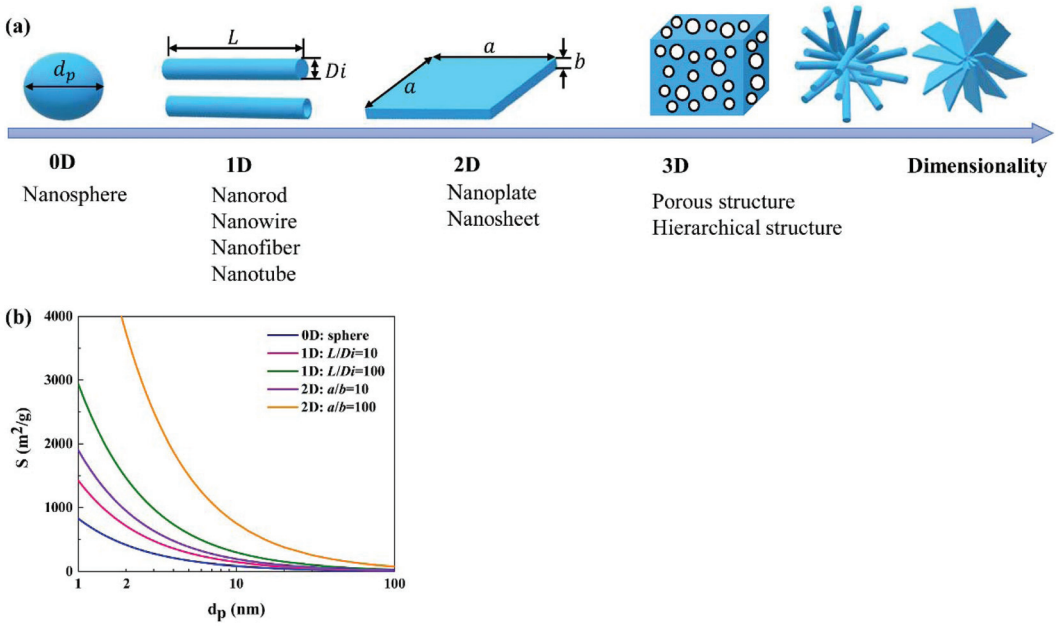

Fig. 12 Schematic illustration of simplified morphologies in 0D, 1D, 2D and 3D (a), and the effect of the particle shape and size on the specific surface area for WO_3 (b).

for photocatalytic reactions, *e.g.*, CO_2 reduction[161] and N_2 fixation.[54]

Elemental doping is commonly achieved by adding the starting material of the dopant (*e.g.* related ions or salts) into the precursor that is used for the synthesis of WO_X. The extent of doping could be easily tuned by varying the addition amount of the dopant source. For instance, Wang *et al.* have performed Mo-doping into $WO_3{\cdot}0.33H_2O$ by adding $Na_2MoO_4{\cdot}2H_2O$ into the $Na_2WO_4{\cdot}2H_2O$ based precursor that is used for the hydrothermal synthesis of $WO_3{\cdot}0.33H_2O$ and modified the extent of doping by adjusting the stoichiometric ratio of Mo : W from 1% to 5%.[161]

Noble metal loading

In the past two decades, loading of noble metal NPs (*e.g.*, Pt,[162] Au[163] and Ag[164]) has received increasing interest for the enhancement of the photocatalytic efficiency of WO_X. WO_3 has been thought to be unsuitable for the efficient oxidative decomposition of organic compounds in air or be limited to the reactions with strong electron acceptors, since its CB is not negative enough for the single-electron reduction of oxygen.[40] In 2008, Abe *et al.* loaded Pt nanoparticles onto the surface of WO_3 and found that the photogenerated electrons in Pt/WO_3 could reduce O_2 through multi-electron reduction ways (*e.g.*, $O_2 + 2H^+ + 2e^- = H_2O_2$ (aq), +0.682 V *vs.* NHE).[40] In these processes, Pt works as an electron pool to accept the photogenerated electrons from WO_3 and as a cocatalyst to facilitate the multi-electron reduction of O_2 to produce H_2O_2. The study by Kim *et al.* has revealed that the reductive decomposition of H_2O_2 produced *in situ* from the reduction of O_2 on the Pt/WO_3 surface is another important path for the generation of $^{\bullet}OH$ radicals, which is an important active species for the degradation of organic compounds.[162] This enhancement mechanism has also been accepted for Au/WO_X and Ag/WO_X composites,[56,165] the typical electron–hole transfer and separation process of which is demonstrated in Fig. 13(a).

The strong LSPR effect induced by noble metal NPs is another important factor contributing to the enhanced photocatalytic efficiency. Surface plasmon resonance (SPR) is a coherent oscillation of the surface conduction electrons excited by an electromagnetic radiation.[166] For the case of LSPR, light interacts with particles much smaller than the incident wavelength.[166] The plasmon frequency of a noble metal NP is correlated with its shape, size and proximity to other nanoparticles. Generally, decreasing the particle size can lead to a reduction in the plasmon frequency, *i.e.* resulting in a redshift of the plasmon resonance absorption.[167] The noble metal

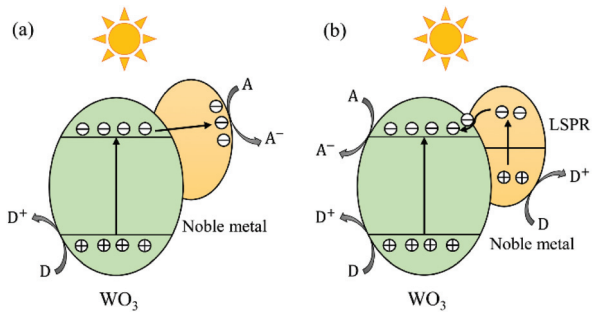

Fig. 13 Schematic illustration of electron–hole transfer and separation in a noble metal loaded WO_3 photocatalyst: the noble metal works as an electron pool (a) and the LSPR effect dominates (b).

NPs loaded on the WO_X surface are generally smaller than 10 nm, corresponding to plasmon resonance absorptions in the visible and NIR regions. When the size of noble metal NPs is reduced to around 2 nm or less, the LSPR would disappear as the band structure becomes discontinuous and breaks down into discrete energy levels.[167] Regarding the plasmonic enhancement in photocatalysis, two mechanisms have been frequently discussed: charge transfer and local electric field enhancement. The mechanism of charge transfer was firstly proposed by Tatsuma's group in 2004 for the study of Au- or Ag-loaded TiO_2 systems.[168] In this mechanism, the plasmon resonance excites electrons in noble metal NPs, which are then transferred to the CB of their adjacent semiconductors, namely the noble metal NPs act as electron-donors (see Fig. 13(b)). This charge transfer mechanism has also been accepted by some authors to explain the enhancement behaviour of noble metal/WO_X photocatalysts.[169] As for the mechanism of local electric field enhancement, studies have revealed that intense local electric fields near the surface of noble metal NPs could be generated by irradiating the NPs near their plasmon resonance frequency. Studies of electromagnetic simulations using the finite-difference time-domain (FDTD) method have shown that the electric field intensity of local plasmonic "hot spots" can reach as much as 1000 times that of the incident electric field.[170] In these "hot spots", the electron–hole pair generation rate is 1000 times that of the incident electromagnetic field. Thus, an increased amount of photoinduced charges is generated locally in the photocatalyst due to the local field enhancement of the plasmonic NPs. This local electric field mechanism has also been adopted by some authors to explain their developed efficient noble metal loaded WO_X photocatalysts.

A uniform distribution of noble metal NPs on the surface of WO_X is always desirable. An excess loading (*i.e.*, more than the optimal level) may lead to agglomeration of the noble metal NPs, thus deteriorating the photocatalytic performance.[169] The optimal loading depends on various factors. Even for the same noble metal, the optimal loading may vary significantly with the morphology of the as-prepared WO_X.[23,57] Nevertheless, the optimal loading of noble metal NPs on the WO_X surface has always be reported to be less than 5 wt% in the literature.

A popular method for the deposition of noble metal NPs onto the WO_X surface is photo-deposition. In a typical process, commercial or as-prepared WO_X particles are added firstly into the aqueous solution of noble metal ions (*e.g.*, $AgNO_3$,[171] H_2PtCl_6 [57] and $HAuCl_4$ [56]), which is then subjected to light irradiation for a certain period of time in the presence of an electron donor (generally methanol). The content and size of the loaded noble metal NPs could be tuned by varying the concentration of the noble metal ion in the solution and/or the intensity and time of the light irradiation. Apart from the *in situ* photo-deposition process, some authors prepared the noble metal colloidal solution firstly, and then immersed the WO_X particles into the as-prepared noble metal colloidal solution. The final noble metal/WO_X composite could be obtained by a post-heat treatment process.[23]

Hybridization with carbon materials

In the past decade, the coupling of WO_X with carbon materials to form highly efficient composite photocatalysts has received increasing interest. Various carbon materials with unique structures have been adopted, such as graphene or reduced graphene oxide (RGO),[58,172] carbon nanotube (CNT) or multi-walled carbon nanotube (MWCNT),[59,173] carbon fiber[172] and carbon nanodot.[60] The carbon material is characterized by excellent electron mobility exceeding ~15 000 $m^2 V^{-1} s^{-1}$, outstanding chemical and thermal stability and strong mechanical strength, which makes it a superior supporting matrix for photocatalysts. In a WO_X/carbon hybrid under illumination, the photogenerated electrons produced in WO_X could be transferred quickly to the carbon material through the interface, leaving photogenerated holes in WO_X. The photogenerated electrons could then react with adsorbed electron-acceptors on the surface of the carbon material. In this way, efficient charge separation is achieved (see Fig. 14).

Amongst the various carbon materials, graphene and RGO (a single layer or multilayer of sp^2 bonded carbon atoms with a honeycomb lattice structure) have attracted much attention due to their ultralight-weight and flexible feature and ultra-large specific surface area (~2600 $m^2 g^{-1}$). RGO is usually obtained by the reduction of graphene oxide (GO), which is commonly prepared by the modified Hummers' method, wherein graphite is used as a starting material and strongly oxidized during a grinding process.[174,175] The oxidation introduces many oxygen-containing functional groups, such as epoxy, hydroxyl, carboxyl and carbonyl groups, on the carbon basal plane, making the obtained GO hydrophilic and easy to disperse stably in water. The oxygen-containing groups on the surface of GO are usually active sites for the growth or deposition of the WO_X catalyst. According to the loading mechanism of WO_X onto the surface of GO, the preparation of WO_X/RGO composites can be categorized into two routes. One is that GO is added into the precursor that is used for the synthesis of WO_X. With this route, WO_X nucleates and grows on the surface of GO during the synthesis process (*e.g.*, a hydrothermal treatment process).[176] Another route is that WO_X is firstly synthesized and then mixed with GO in solution fol-

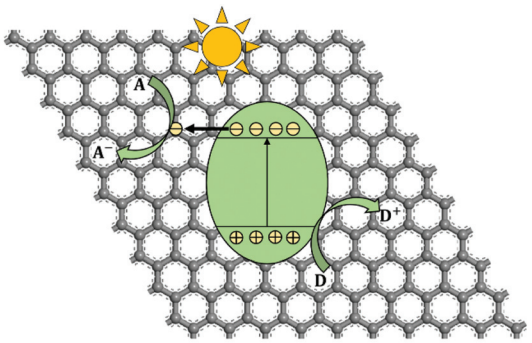

Fig. 14 Schematic illustration of the charge transfer and separation in a WO_X/carbon photocatalyst.

lowed by a specific treatment that allows the deposition of WO_X onto the surface of GO. The GO in the as-prepared WO_X/GO composite could then be reduced to RGO by a thermal decomposition or by specific reduction processes (*e.g.*, a chemical reduction using hydrazine vapor at 90 °C for 24 h).[177]

Coupling with other semiconductors

Coupling WO_X with other semiconductors having unequal band structures is an effective way to facilitate charge transfer and separation and to improve photo-induced redox ability. In the literature, various semiconductors (*e.g.*, chalcogenides, halogenides, salts and carbon nitrides) have been reported to construct heterojunctions with WO_X to form efficient photocatalysts, such as WO_X/TiO_2,[178–180] WO_3/Fe_2O_3,[181,182] WO_3/Cu_2O,[61,183] WO_3/ZnO,[96,184] WO_3/CdS,[185,186] WO_3/Bi_2S_3,[187,188] $WO_3/ZnIn_2S_2$,[189] WO_3/AgI,[190] $WO_3/BiOCl_{0.25}Br_{0.75}$,[191] WO_3/BiOI,[95] WO_3/Ag_3PO_4,[62,192] $WO_3/BiVO_4$,[193,194] $WO_3/NiWO_4$,[195] WO_3/Bi_2WO_6,[196,197] WO_X/g-C_3N_4,[198–200] *etc*. For the ease of comparison, the electronic band structures of WO_3 and its typical coupled semiconductors are summarized in Fig. 15. According to the mechanism of charge transfer, the WO_X/semiconductor photocatalysts can be categorized into two groups: conventional type-II and *Z*-scheme (see Fig. 16). In a conventional type-II heterojunction, the photogenerated electrons transfer from the CB of the coupled semiconductor to that of WO_X with the photogenerated holes migrating from the VB of WO_X to that of the coupled semiconductor. Therefore, the photoreduction occurs on the surface of WO_X while the photooxidation takes place on the surface of the coupled semiconductor. With this configuration, efficient spatial separation of electron–hole pairs could be obtained, however, the photooxidizing ability of the composite is decreased to some extent when compared to that of bare WO_X. In a *Z*-scheme heterojunction, the photogenerated electrons from WO_X recombine with the holes in the coupled semiconductor, while the holes in WO_X and the electrons in the coupled semiconductor remain separated and reactive. In this case, the heterojunction retains the strong photo-oxidizing ability of WO_X and possesses a higher photo-reducing ability imparted by the coupled semiconductor. As both types of the heterojunction have a staggered band structure, the charge transfer mechanism for a specific composite needs to be confirmed by experiment, *e.g.*, detection of active species during a photocatalytic reaction. For some WO_X/semiconductor systems (*e.g.*, WO_3/Cu_2O, WO_3/TiO_2 and WO_3/Fe_2O_3), the mechanism of charge transfer may alter depending on the synthesis routes and the applied photocatalytic reactions. For instance, Zhang *et al.* have prepared a WO_3/Cu_2O photoanode for PEC water splitting *via* a hydrothermal method followed by electrodeposition.[183] The charge transfer in this heterojunction has been reported to follow the conventional type-II mode. However, in the study of Shi *et al.*[61] where a WO_3/Cu_2O composite was synthesized using similar procedures but applied for CO_2 reduction, the charge transfer was confirmed to follow the *Z*-scheme mechanism.

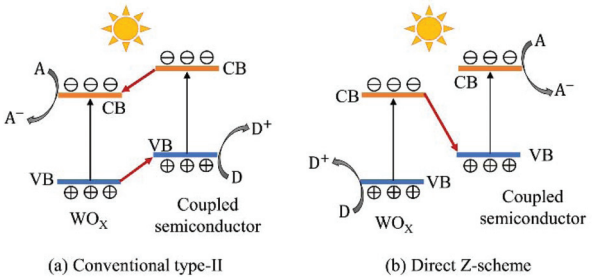

Fig. 16 Schematic illustration of electron–hole transfer and separation in conventional type-II (a) and *Z*-scheme (b) WO_X/semiconductor heterojunction photocatalysts.

Apart from the necessity of unequal band structures, intimate contact is another basic requirement for the efficient separation of charge carriers. In addition, the optimization of the contact surface area between WO_X and the coupled semiconductor is also important to intensify the overall photocatalytic efficiency. This has been achieved by various unique morphology designs, such as the 0D/1D (*e.g.* Bi_2WO_6 NPs decorated on WO_3 nanorods),[197] 0D/2D (*e.g.* $BiVO_4$ NPs anchored on WO_3 nanoplates),[194] 0D/3D (*e.g.* Ag_3PO_4 NPs dispersed in 3D ordered microporous WO_3),[201] 1D/2D (*e.g.* $W_{18}O_{49}$ nanowires dispersed on g-C_3N_4 nanosheets)[198] and 2D/2D (*e.g.* WO_3 nanoplates on g-C_3N_4 nanosheets)[63] structures, *etc*.

The construction of WO_X/semiconductor heterojunctions could be achieved by a one-step or two-step preparation

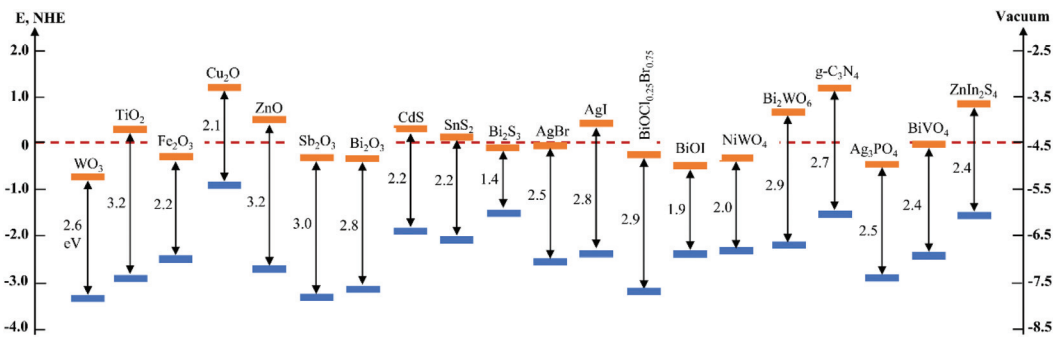

Fig. 15 CB and VB energy levels of WO_3 and a number of semiconductors.

method. In a one-step method, the starting materials for both WO_X and the coupled semiconductor are generally mixed in a precursor solution and then used for a synthesis process. For instance, Zhou *et al.* have prepared a $WO_3/BiWO_6$ composite *via* a one-step hydrothermal method using a precursor containing both $Bi(NO_3)_3{\cdot}5H_2O$ and H_2WO_4.[202] Compared to the one-step method, the two-step methods are more commonly adopted. In a two-step method, one semiconductor (*i.e.* WO_X or the coupled semiconductor) is generally synthesized firstly and then mixed with the precursor solution that is used for the synthesis of the second semiconductor. The deposition and growth of the second semiconductor onto the surface of the first semiconductor could be achieved by using various synthesis methods. For instance, Ye and Wen have prepared a $WO_3/ZnIn_2S_4$ composite by synthesizing firstly the WO_3 nanorods *via* a hydrothermal process and then mixed the as-synthesized WO_3 nanorods with the precursor solution containing $In(NO_3)_3{\cdot}4.5H_2O$, $Zn(AC)_2{\cdot}6H_2O$ and $C_3H_7NO_2S{\cdot}HCl{\cdot}H_2O$ followed by another hydrothermal treatment, which allows the deposition and growth of $ZnIn_2S_4$ on the surface of WO_3.[189] The WO_X and the coupled semiconductor could also be synthesized firstly and separately and then mixed in a solution followed by a specific treatment to allow intimate contact. For instance, Lara *et al.* have performed the coupling of WO_3 and TiO_2 by mixing the as-synthesized WO_3 and TiO_2 in a solution followed by a second-step hydrothermal treatment.[179]

Conclusions and perspectives

This review summarizes firstly the fundamentals of WO_X (*i.e.* crystal and electronic structures and optical properties) and then highlights the strategies for the enhancement of the photocatalytic efficiency of WO_X-based photocatalysts. These include the controls in the crystal phase, stoichiometry/oxygen-vacancy, active facet and morphology, elemental doping, loading of noble metal NPs, hybridization with carbon materials and coupling with other semiconductors to construct heterojunctions.

For nanostructured WO_X, not only the monoclinic I phase but also the hexagonal, orthorhombic and triclinic phases could retain phase stability and exhibit photocatalytic activity at room temperature. Taking advantage of the polymorphic property of WO_X, a phase junction could be formed to facilitate the transfer and separation of photogenerated charge carriers. Compared to stoichiometric WO_3, oxygen-deficient WO_{3-x} exhibits extended light absorption in the visible and NIR regions and possesses a higher density of free charge carriers, both of which are beneficial for improving the photocatalytic performance. {002} is the active facet of m- and o-WO_X due to their high surface energy. A morphology with a high percentage of exposed active facets and large specific surface area is always desirable, which could be best achieved by a 2D structure with a high aspect ratio. The WO_X with 3D hierarchical structures assembled by 1D and/or 2D building blocks and 3D ordered macroporous structures are also applausive for practical applications due to their high structural stability and less agglomeration. Doping WO_X with low valence metal ions could extend light absorption, promote photo-induced electron–hole separation and improve photocatalytic redox ability due to the increased oxygen vacancies and the introduced defect band. By loading noble metal NPs onto the surface of WO_X, it is possible to extend light absorption into the visible and NIR regions and provide large numbers of "hot electrons" to participate in photocatalytic reactions, which is due to the strong LSPR effect. Graphene is an ideal support for the WO_X photocatalyst, for it provides an ultra-large specific surface area and serves as an excellent conductor for photogenerated electrons migrating from WO_X. Coupling WO_X with other semiconductors having unequal band structures could achieve efficient spatial charge separation *via* facilitating the charge transfer through the interfaces. By the construction of a *Z*-scheme heterojunction, the strong photo-oxidation ability of WO_X can be retained while the photo-reduction ability could be enhanced because of the higher CB level of the coupled semiconductor.

However, the photocatalytic efficiency of WO_X-based photocatalysts is still far from expectation, further improvement of which might rely on controls in synergistic effects. Combining different strategies (*e.g.* controls in the crystal phase, stoichiometry, active facet and morphology and coupling with other materials) in unique ways might lead to incredible results that could not be obtained with single strategies. To achieve the effective control of synergistic effects, the mechanisms of single strategies should be clear, some of which, however, are still vague. For instance, the charge transfer mechanism in the noble metal loaded system is still inconsistent. Furthermore, theoretical guidelines for the construction of *Z*-scheme heterojunctions are still lacking. The final aim of the development of efficient photocatalysts is to serve human beings by solving practical problems. However, the research of WO_X-based photocatalysts is still limited to laboratories. The efforts contributing to exploit appropriate ways for practical applications of WO_X-based photocatalysts, *e.g.*, design of photo-reactors and integration with other technologies to extend applications, should be highlighted in the future.

Conflicts of interest

There are no conflicts to declare.

Acknowledgements

This work was partly supported by the Ministry of Science and Technology of China (2016YFB0303901-05). Y. Gao acknowledges the funding from the Changjiang Scholars Programs (T2015136). W. Wang acknowledges the National Natural Science Foundation of China (51772312, 21671197).

References

1 A. A. Ismail and D. W. Bahnemann, Photochemical splitting of water for hydrogen production by photocatalysis: A review, *Sol. Energy Mater. Sol. Cells*, 2014, **128**, 85–101.

2 H. Ahmad, S. K. Kamarudin, L. J. Minggu and M. Kassim, Hydrogen from photo-catalytic water splitting process: A review, *Renewable Sustainable Energy Rev.*, 2015, **43**, 599–610.

3 S. Sun, X. Zhang, X. Liu, L. Pan, X. Zhang and J. Zou, Design and Construction of Cocatalysts for Photocatalytic Water Splitting, *Acta Phys.-Chim. Sin.*, 2020, **36**, 1905007.

4 X. Xu, L. Pan, X. Zhang, L. Wang and J. Zou, Rational Design and Construction of Cocatalysts for Semiconductor-Based Photo-Electrochemical Oxygen Evolution: A Comprehensive Review, *Adv. Sci.*, 2019, **6**, 1801505.

5 Y. C. Zhang, N. Afzal, L. Pan, X. Zhang and J. J. Zou, Structure-Activity Relationship of Defective Metal-Based Photocatalysts for Water Splitting: Experimental and Theoretical Perspectives, *Adv. Sci.*, 2019, **6**, 1900053.

6 S. Sun, G. Shen, J. Jiang, W. Mi, X. Liu, L. Pan, X. Zhang and J. J. Zou, Boosting Oxygen Evolution Kinetics by Mn–N–C Motifs with Tunable Spin State for Highly Efficient Solar-Driven Water Splitting, *Adv. Energy Mater.*, 2019, **9**, 1901505.

7 O. Ola and M. M. Maroto-Valer, Review of material design and reactor engineering on TiO_2 photocatalysis for CO_2 reduction, *J. Photochem. Photobiol., C*, 2015, **24**, 16–42.

8 N. Shehzad, M. Tahir, K. Johari, T. Murugesan and M. Hussain, A critical review on TiO_2 based photocatalytic CO_2 reduction system: Strategies to improve efficiency, *J. CO_2 Util.*, 2018, **26**, 98–122.

9 X. Chen, N. Li, Z. Kong, W. Ong and X. Zhao, Photocatalytic fixation of nitrogen to ammonia: state-of-the-art advancements and future prospects, *Mater. Horiz.*, 2018, **5**, 9–27.

10 M. N. Chong, B. Jin, C. W. K. Chow and C. Saint, Recent developments in photocatalytic water treatment technology: A review, *Water Res.*, 2010, **44**, 2997–3027.

11 H. Zangeneh, A. A. L. Zinatizadeh, M. Habibi, M. Akia and M. Hasnain Isa, Photocatalytic oxidation of organic dyes and pollutants in wastewater using different modified titanium dioxides: A comparative review, *J. Ind. Eng. Chem.*, 2015, **26**, 1–36.

12 Y. Boyjoo, H. Sun, J. Liu, V. K. Pareek and S. Wang, A review on photocatalysis for air treatment: From catalyst development to reactor design, *Chem. Eng. J.*, 2017, **310**, 537–559.

13 Z. Shayegan, C. Lee and F. Haghighat, TiO_2 photocatalyst for removal of volatile organic compounds in gas phase-A review, *Chem. Eng. J.*, 2018, **334**, 2408–2439.

14 M. Cheng, G. Zeng, D. Huang, C. Lai, P. Xu, C. Zhang and Y. Liu, Hydroxyl radicals based advanced oxidation processes (AOPs) for remediation of soils contaminated with organic compounds: A review, *Chem. Eng. J.*, 2016, **284**, 582–598.

15 S. Banerjee, D. D. Dionysiou and S. C. Pillai, Self-cleaning applications of TiO_2 by photo-induced hydrophilicity and photocatalysis, *Appl. Catal., B*, 2015, **176–177**, 396–428.

16 P. Ganguly, C. Byrne, A. Breen and S. C. Pillai, Antimicrobial activity of photocatalysts: Fundamentals, mechanisms, kinetics and recent advances, *Appl. Catal., B*, 2018, **225**, 51–75.

17 C. Zhang, Y. Li, D. Shuai, Y. Shen and D. Wang, Progress and challenges in photocatalytic disinfection of waterborne Viruses: A review to fill current knowledge gaps, *Chem. Eng. J.*, 2019, **355**, 399–415.

18 A. L. Linsebigler, G. Lu and J. T. Yates, Photocatalysis on TiO_2 Surfaces: Principles, Mechanisms, and Selected Results, *Chem. Rev.*, 1995, **95**, 735–758.

19 K. Nakata and A. Fujishima, TiO_2 photocatalysis: Design and applications, *J. Photochem. Photobiol., C*, 2012, **13**, 169–189.

20 J. Low, J. Yu, M. Jaroniec, S. Wageh and A. A. Al-Ghamdi, Heterojunction Photocatalysts, *Adv. Mater.*, 2017, **29**, 1601694.

21 A. Fujishima, T. N. Rao and D. A. Tryk, Titanium dioxide photocatalysis, *J. Photochem. Photobiol., C*, 2000, **1**, 1–21.

22 A. Fujishima, X. Zhang and D. Tryk, TiO_2 photocatalysis and related surface phenomena, *Surf. Sci. Rep.*, 2008, **63**, 515–582.

23 Z. Zhao and M. Miyauchi, Nanoporous-Walled Tungsten Oxide Nanotubes as Highly Active Visible-Light-Driven Photocatalysts, *Angew. Chem., Int. Ed.*, 2008, **47**, 7051–7055.

24 H. Irie, Y. Watanabe and K. Hashimoto, Carbon-doped Anatase TiO_2 Powders as a Visible-light Sensitive Photocatalyst, *Chem. Lett.*, 2003, **32**, 772–773.

25 T. Ohno, T. Mitsui and M. Matsumura, Photocatalytic Activity of S-doped TiO_2 Photocatalyst under Visible Light, *Chem. Lett.*, 2003, **32**, 364–365.

26 V. Etacheri, C. Di Valentin, J. Schneider, D. Bahnemann and S. C. Pillai, Visible-light activation of TiO_2 photocatalysts: Advances in theory and experiments, *J. Photochem. Photobiol., C*, 2015, **25**, 1–29.

27 S. Sakthivel, M. Janczarek and H. Kisch, Visible Light Activity and Photoelectrochemical Properties of Nitrogen-Doped TiO_2, *J. Phys. Chem. B*, 2004, **108**, 19384–19387.

28 S. G. Ullattil, S. B. Narendranath, S. C. Pillai and P. Periyat, Black TiO_2 Nanomaterials: A Review of Recent Advances, *Chem. Eng. J.*, 2018, **343**, 708–736.

29 P. Dong, G. Hou, X. Xi, R. Shao and F. Dong, WO_3-based photocatalysts: morphology control, activity enhancement and multifunctional applications, *Environ. Sci.: Nano*, 2017, **4**, 539–557.

30 M. Mishra and D. Chun, α-Fe_2O_3 as a photocatalytic material: A review, *Appl. Catal., A*, 2015, **498**, 126–141.

31 N. Bao, L. Shen, T. Takata and K. Domen, Self-Templated Synthesis of Nanoporous CdS Nanostructures for Highly Efficient Photocatalytic Hydrogen Production under Visible Light, *Chem. Mater.*, 2008, **20**, 110–117.

32 S. Tokunaga, H. Kato and A. Kudo, Selective Preparation of Monoclinic and Tetragonal $BiVO_4$ with Scheelite

Structure and Their Photocatalytic Properties, *Chem. Mater.*, 2001, **13**, 4624–4628.
33 H. Fu, C. Pan, W. Yao and Y. Zhu, Visible-Light-Induced Degradation of Rhodamine B by Nanosized Bi_2WO_6, *J. Phys. Chem. B*, 2005, **109**, 22432–22439.
34 M. Shang, W. Wang, S. Sun, L. Zhou and L. Zhang, Bi_2WO_6 Nanocrystals with High Photocatalytic Activities under Visible Light, *J. Phys. Chem. C*, 2008, **112**, 10407–10411.
35 Z. Yi, J. Ye, N. Kikugawa, T. Kako, S. Ouyang, H. Stuart-Williams, H. Yang, J. Cao, W. Luo, Z. Li, Y. Liu and R. L. Withers, An orthophosphate semiconductor with photooxidation properties under visible-light irradiation, *Nat. Mater.*, 2010, **9**, 559–564.
36 J. Wen, J. Xie, X. Chen and X. Li, A review on g-C_3N_4-based photocatalysts, *Appl. Surf. Sci.*, 2017, **391**, 72–123.
37 Z. Huang, J. Song, L. Pan, X. Zhang, L. Wang and J. Zou, Tungsten Oxides for Photocatalysis, Electrochemistry, and Phototherapy, *Adv. Mater.*, 2015, **27**, 5309–5327.
38 S. S. Kalanur, I. Yoo, I. Cho and H. Seo, Effect of oxygen vacancies on the band edge properties of WO_3 producing enhanced photocurrents, *Electrochim. Acta*, 2019, **296**, 517–527.
39 T. Soltani, A. Tayyebi and B. Lee, Sonochemical-driven ultrafast facile synthesis of WO_3 nanoplates with controllable morphology and oxygen vacancies for efficient photoelectrochemical water splitting, *Ultrason. Sonochem.*, 2019, **50**, 230–238.
40 R. Abe, H. Takami, N. Murakami and B. Ohtani, Pristine Simple Oxides as Visible Light Driven Photocatalysts: Highly Efficient Decomposition of Organic Compounds over Platinum-Loaded Tungsten Oxide, *J. Am. Chem. Soc.*, 2008, **130**, 7780–7781.
41 Y. Li, Z. Tang, J. Zhang and Z. Zhang, Fabrication of vertical orthorhombic/hexagonal tungsten oxide phase junction with high photocatalytic performance, *Appl. Catal., B*, 2017, **207**, 207–217.
42 D. B. Hernandez-Uresti, D. Sánchez-Martínez, A. Martínez-de La Cruz, S. Sepúlveda-Guzmán and L. M. Torres-Martínez, Characterization and photocatalytic properties of hexagonal and monoclinic WO_3 prepared via microwave-assisted hydrothermal synthesis, *Ceram. Int.*, 2014, **40**, 4767–4775.
43 Y. Kong, H. Sun, X. Zhao, B. Gao and W. Fan, Fabrication of hexagonal/cubic tungsten oxide homojunction with improved photocatalytic activity, *Appl. Catal., A*, 2015, **505**, 447–455.
44 R. Zhang, F. Ning, S. Xu, L. Zhou, M. Shao and M. Wei, Oxygen vacancy engineering of WO_3 toward largely enhanced photoelectrochemical water splitting, *Electrochim. Acta*, 2018, **274**, 217–223.
45 Y. Wang, J. Cai, M. Wu, J. Chen, W. Zhao, Y. Tian, T. Ding, J. Zhang, Z. Jiang and X. Li, Rational construction of oxygen vacancies onto tungsten trioxide to improve visible light photocatalytic water oxidation reaction, *Appl. Catal., B*, 2018, **239**, 398–407.
46 J. Zhang, P. Zhang, T. Wang and J. Gong, Monoclinic WO_3 nanomultilayers with preferentially exposed (002) facets for photoelectrochemical water splitting, *Nano Energy*, 2015, **11**, 189–195.
47 Y. Li, Z. Tang, J. Zhang and Z. Zhang, Exposed facet and crystal phase tuning of hierarchical tungsten oxide nanostructures and their enhanced visible-light-driven photocatalytic performance, *CrystEngComm*, 2015, **17**, 9102–9110.
48 X. Wang, H. Fan and P. Ren, Effects of exposed facets on photocatalytic properties of WO_3, *Adv. Powder Technol.*, 2017, **28**, 2549–2555.
49 M. Aslam, I. M. I. Ismail, S. Chandrasekaran and A. Hameed, Morphology controlled bulk synthesis of disc-shaped WO_3 powder and evaluation of its photocatalytic activity for the degradation of phenols, *J. Hazard. Mater.*, 2014, **276**, 120–128.
50 Y. Liang, Y. Yang, C. Zou, K. Xu, X. Luo, T. Luo, J. Li, Q. Yang, P. Shi and C. Yuan, 2D ultra-thin WO_3 nanosheets with dominant {002} crystal facets for high-performance xylene sensing and methyl orange photocatalytic degradation, *J. Alloys Compd.*, 2019, **783**, 848–854.
51 Z. Wang, D. Chu, L. Wang, L. Wang, W. Hu, X. Chen, H. Yang and J. Sun, Facile synthesis of hierarchical double-shell WO_3 microspheres with enhanced photocatalytic activity, *Appl. Surf. Sci.*, 2017, **396**, 492–496.
52 J. O. Tijani, O. Ugochukwu, L. A. Fadipe, M. T. Bankole, A. S. Abdulkareem and W. D. Roos, Photocatalytic degradation of local dyeing wastewater by iodine-phosphorus co-doped tungsten trioxide nanocomposites under natural sunlight irradiation, *J. Environ. Manage.*, 2019, **236**, 519–533.
53 S. S. Kalanur, I. Yoo, I. S. Cho and H. Seo, Niobium incorporated WO_3 nanotriangles: Band edge insights and improved photoelectrochemical water splitting activity, *Ceram. Int.*, 2019, **45**, 8157–8165.
54 Z. Ying, S. Chen, S. Zhang, T. Peng and R. Li, Efficiently enhanced N_2 photofixation performance of sea-urchin-like $W_{18}O_{49}$ microspheres with Mn-doping, *Appl. Catal., B*, 2019, **254**, 351–359.
55 Y. Liu, Z. Zhang, Y. Fang, B. Liu, J. Huang, F. Miao, Y. Bao and B. Dong, IR-Driven strong plasmonic-coupling on Ag nanorices/$W_{18}O_{49}$ nanowires heterostructures for photo/thermal synergistic enhancement of H_2 evolution from ammonia borane, *Appl. Catal., B*, 2019, **252**, 164–173.
56 D. P. DePuccio, P. Botella, B. O. Rourke and C. C. Landry, Degradation of Methylene Blue Using Porous WO_3, SiO_2-WO_3, and Their Au-Loaded Analogs: Adsorption and Photocatalytic Studies, *ACS Appl. Mater. Interfaces*, 2015, **7**, 1987–1996.
57 H. Widiyandari, A. Purwanto, R. Balgis, T. Ogi and K. Okuyama, CuO/WO_3 and Pt/WO_3 nanocatalysts for efficient pollutant degradation using visible light irradiation, *Chem. Eng. J.*, 2012, **180**, 323–329.
58 L. Tie, C. Yu, Y. Zhao, H. Chen, S. Yang, J. Sun, S. Dong and J. Sun, Fabrication of WO_3 nanorods on reduced graphene oxide sheets with augmented visible light photo-

catalytic activity for efficient mineralization of dye, *J. Alloys Compd.*, 2018, **769**, 83–91.
59 W. Zhu, Z. Li, C. He, S. Faqian and Y. Zhou, Enhanced photodegradation of sulfamethoxazole by a novel WO_3-CNT composite under visible light irradiation, *J. Alloys Compd.*, 2018, **754**, 153–162.
60 J. Zhang, Y. Ma, Y. Du, H. Jiang, D. Zhou and S. Dong, Carbon nanodots/WO_3 nanorods Z-scheme composites: Remarkably enhanced photocatalytic performance under broad spectrum, *Appl. Catal., B*, 2017, **209**, 253–264.
61 W. Shi, X. Guo, C. Cui, K. Jiang, Z. Li, L. Qu and J. Wang, Controllable synthesis of Cu_2O decorated WO_3 nanosheets with dominant (0 0 1) facets for photocatalytic CO_2 reduction under visible-light irradiation, *Appl. Catal., B*, 2019, **243**, 236–242.
62 X. Liu, J. Xu, Z. Ni, R. Wang, J. You and R. Guo, Adsorption and visible-light-driven photocatalytic properties of Ag_3PO_4/WO_3 composites: A discussion of the mechanism, *Chem. Eng. J.*, 2019, **356**, 22–33.
63 J. Fu, Q. Xu, J. Low, C. Jiang and J. Yu, Ultrathin 2D/2D WO_3/g-C_3N_4 step-scheme H2-production photocatalyst, *Appl. Catal., B*, 2019, **243**, 556–565.
64 T. Zhu, M. N. Chong and E. S. Chan, Nanostructured Tungsten Trioxide Thin Films Synthesized for Photoelectrocatalytic Water Oxidation: A review, *ChemSusChem*, 2014, **7**, 2974–2997.
65 M. B. Tahir, G. Nabi, M. Rafique and N. R. Khalid, Nanostructured-based WO_3 photocatalysts: recent development, activity enhancement, perspectives and applications for wastewater treatment, *Int. J. Environ. Sci. Technol.*, 2017, **14**, 2519–2542.
66 P. M. Woodward, A. W. Sleight and T. Vogt, Ferroelectric Tungsten Trioxide, *J. Solid State Chem.*, 1997, **131**, 9–17.
67 F. Corà, A. Patel, N. M. Harrison, R. Dovesi and C. R. A. Catlow, An ab Initio Hartree–Fock Study of the Cubic and Tetragonal Phases of Bulk Tungsten Trioxide, *J. Am. Chem. Soc.*, 1996, **118**, 12174–12182.
68 R. Diehl, G. Brandt and E. Salje, The crystal structure of triclinic WO_3, *Acta Crystallogr., Sect. B: Struct. Crystallogr. Cryst. Chem.*, 1978, **34**, 1105–1111.
69 E. Salje, The orthorhombic phase of WO_3, *Acta Crystallogr., Sect. B: Struct. Crystallogr. Cryst. Chem.*, 1977, **33**, 574–577.
70 W. L. Kehl, R. G. Hay and D. Wahl, The Structure of Tetragonal Tungsten Trioxide, *J. Appl. Phys.*, 1952, **23**, 212–215.
71 S. Tanisaki, Crystal Structure of Monoclinic Tungsten Trioxide at Room Temperature, *J. Phys. Soc. Jpn.*, 1960, **15**, 573–581.
72 K. R. Locherer, I. P. Swainson and E. K. H. Salje, Transition to a new tetragonal phase of WO_3: crystal structure and distortion parameters, *J. Phys.: Condens. Matter*, 1999, **11**, 4143–4156.
73 T. Vogt, P. M. Woodward and B. A. Hunter, The High-Temperature Phases of WO_3, *J. Solid State Chem.*, 1999, **144**, 209–215.
74 H. Zheng, J. Z. Ou, M. S. Strano, R. B. Kaner, A. Mitchell and K. Kalantar-zadeh, Nanostructured Tungsten Oxide-Properties, Synthesis, and Applications, *Adv. Funct. Mater.*, 2011, **21**, 2175–2196.
75 S. Adhikari, R. Swain, D. Sarkar and G. Madras, Wedge-like WO_3 architectures for efficient electrochromism and photoelectrocatalytic activity towards water pollutants, *Mol. Catal.*, 2017, **432**, 76–87.
76 K. Hayat, M. A. Gondal, M. M. Khaled, Z. H. Yamani and S. Ahmed, Laser induced photocatalytic degradation of hazardous dye (Safranin-O) using self synthesized nanocrystalline WO_3, *J. Hazard. Mater.*, 2011, **186**, 1226–1233.
77 S. Yao, F. Qu, G. Wang and X. Wu, Facile hydrothermal synthesis of WO_3 nanorods for photocatalysts and supercapacitors, *J. Alloys Compd.*, 2017, **724**, 695–702.
78 B. Gerand, G. Nowogrocki, J. Guenot and M. Figlarz, Structural Study of a New Hexagonal Form of Tungsten Trioxide, *J. Solid State Chem.*, 1979, **29**, 429–434.
79 B. G. Hyde, A. N. Bagshaw, S. Andersson and M. O'Keeffe, Some Defect Structures in Crystalline Solids, *Annu. Rev. Mater. Sci.*, 1974, **4**, 43–49.
80 A. Magnéli, Structures of the ReO_3-type with recurrent dislocations of atoms: 'homologous series' of molybdenum and tungsten oxides, *Acta Crystallogr.*, 1953, **6**, 495–500.
81 M. Lundberg, M. Sundberg and A. Magneli, The "Pentagonal Column" as a Building Unit in Crystal and Defect Structures of Some Groups of Transition Metal Compounds, *J. Solid State Chem.*, 1982, **44**, 32–40.
82 D. B. Migas, V. L. Shaposhnikov and V. E. Borisenko, Tungsten oxides. II. The metallic nature of Magnéli phases, *J. Appl. Phys.*, 2010, **108**, 093714.
83 X. Fang, M. Yao, L. Guo, Y. Xu, W. Zhou, M. Zhuo, C. Shi, L. Liu, L. Wang, X. Li and W. Chen, One-Step, Solventless, and Scalable Mechanosynthesis of $WO_3{\cdot}2H_2O$ Ultrathin Narrow Nanosheets with Superior UV-Vis-Light-Driven Photocatalytic Activity, *ACS Sustainable Chem. Eng.*, 2017, **5**, 10735–10743.
84 Q. Zeng, Y. Zhao, J. Zhao, X. Hao, Y. Lu, J. Guo, Y. Song, F. Gao and Z. Huang, Studies on fabrication of urchin-like $WO_3{\cdot}H_2O$ hollow spheres and their photocatalytic properties, *Cryst. Res. Technol.*, 2013, **48**, 334–343.
85 J. Ke, H. Zhou, J. Liu, X. Duan, H. Zhang, S. Liu and S. Wang, Crystal transformation of 2D tungstic acid H_2WO_4 to WO_3 for enhanced photocatalytic water oxidation, *J. Colloid Interface Sci.*, 2018, **514**, 576–583.
86 X. Wang, X. Meng, M. Zhong, F. Wu and J. Li, Hydrothermal synthesis of $WO_3{\cdot}0.5H_2O$ microtubes with excellent photocatalytic properties, *Appl. Surf. Sci.*, 2013, **282**, 826–831.
87 X. Song, C. Wang, W. Wang, X. Zhang, N. Hou and H. Yu, A Dissolution-Regeneration Route to Synthesize Blue Tungsten Oxide Flowers and their Applications in Photocatalysis and Gas Sensing, *Adv. Mater. Interfaces*, 2016, **3**, 1500417.
88 Y. Tanaka, M. Miyayama, M. Hibino and T. Kudo, Preparation and proton conductivity of $WO_3{\cdot}2H_2O$/

epoxy composite films, *Solid State Ionics*, 2004, **171**, 33–39.

89 L. Li, J. Zhao, Y. Wang, Y. Li, D. Ma, Y. Zhao, S. Hou and X. Hao, Oxalic acid mediated synthesis of $WO_3 \cdot H_2O$ nanoplates and self-assembled nanoflowers under mild conditions, *J. Solid State Chem.*, 2011, **184**, 1661–1665.

90 J. Yang, W. Li, J. Li, D. Sun and Q. Chen, Hydrothermal synthesis and photoelectrochemical properties of vertically aligned tungsten trioxide (hydrate) plate-like arrays fabricated directly on FTO substrates, *J. Mater. Chem.*, 2012, **22**, 17744.

91 J. R. Gunter, M. Amberg and H. Schmalle, Direct synthesis and single crystal structure determination of cubic pyrochlore-type tungsten trioxide hemihydrate, $WO_3 \cdot 0.5H_2O$, *Mater. Res. Bull.*, 1989, **24**, 289–292.

92 S. S. Kalanur and H. Seo, Intercalation of barium into monoclinic tungsten oxide nanoplates for enhanced photoelectrochemical water splitting, *Chem. Eng. J.*, 2019, **355**, 784–796.

93 L. Zhou, J. Zou, M. Yu, P. Lu, J. Wei, Y. Qian, Y. Wang and C. Yu, Green Synthesis of Hexagonal-Shaped $WO_3 \cdot 0.33H_2O$ Nanodiscs Composed of Nanosheets, *Cryst. Growth Des.*, 2008, **8**, 3993–3998.

94 S. Cong, F. Geng and Z. Zhao, Tungsten Oxide Materials for Optoelectronic Applications, *Adv. Mater.*, 2016, **28**, 10518–10528.

95 J. Luo, X. Zhou, L. Ma and X. Xu, Enhanced visible-light-driven photocatalytic activity of WO_3/BiOI heterojunction photocatalysts, *J. Mol. Catal. A: Chem.*, 2015, **410**, 168–176.

96 R. Lei, H. Zhang, H. Ni, R. Chen, H. Gu and B. Zhang, Novel ZnO nanoparticles modified WO_3 nanosheet arrays for enhanced photocatalytic properties under solar light illumination, *Appl. Surf. Sci.*, 2019, **463**, 363–373.

97 X. Chen, S. Shen, L. Guo and S. S. Mao, Semiconductor-based Photocatalytic Hydrogen Generation, *Chem. Rev.*, 2010, **110**, 6503–6570.

98 T. Paik, M. Cargnello, T. R. Gordon, S. Zhang, H. Yun, J. D. Lee, H. Y. Woo, S. J. Oh, C. R. Kagan, P. Fornasiero and C. B. Murray, Photocatalytic Hydrogen Evolution from Substoichiometric Colloidal WO_{3-x} Nanowires, *ACS Energy Lett.*, 2018, **3**, 1904–1910.

99 S. K. Gullapalli, R. S. Vemuri and C. V. Ramana, Structural transformation induced changes in the optical properties of nanocrystalline tungsten oxide thin films, *Appl. Phys. Lett.*, 2010, **96**, 171903.

100 L. Brus, Electronic wave functions in semiconductor clusters: experiment and theory, *J. Phys. Chem.*, 1986, **90**, 2555–2560.

101 W. Yu, J. Chen, T. Shang, L. Chen, L. Gu and T. Peng, Direct Z-scheme g-C_3N_4-WO_3 photocatalyst with atomically defined junction for H_2 production, *Appl. Catal., B*, 2017, **219**, 693–704.

102 H. Watanabe, K. Fujikata, Y. Oaki and H. Imai, Band-gap expansion of tungsten oxide quantum dots synthesized in sub-nano porous silica, *Chem. Commun.*, 2013, **49**, 8477–8479.

103 A. Polaczek, M. Pekala and Z. Obuszko, Magnetic susceptibility and thermoelectric power of tungsten intermediary oxides, *J. Phys.: Condens. Matter*, 1994, **6**, 7909–7919.

104 S. K. Deb, Opportunities and challenges in science and technology of WO_3 for electrochromic and related applications, *Sol. Energy Mater. Sol. Cells*, 2008, **92**, 245–258.

105 Y. Li, Z. Tang, J. Zhang and Z. Zhang, Defect Engineering of Air-Treated WO_3 and Its Enhanced Visible-Light-Driven Photocatalytic and Electrochemical Performance, *J. Phys. Chem. C*, 2016, **120**, 9750–9763.

106 G. Hai, J. Huang, L. Cao, Y. Jie, J. Li, X. Wang and G. Zhang, Influence of oxygen deficiency on the synthesis of tungsten oxide and the photocatalytic activity for the removal of organic dye, *J. Alloys Compd.*, 2017, **690**, 239–248.

107 B. Ahmed, S. Kumar, A. K. Ojha, P. Donfack and A. Materny, Facile and controlled synthesis of aligned WO_3 nanorods and nanosheets as an efficient photocatalyst material, *Spectrochim. Acta, Part A*, 2017, **175**, 250–261.

108 J. Z. Ou, R. A. Rani, S. Balendhran, A. S. Zoolfakar, M. R. Field, S. Zhuiykov, A. P. O'Mullane and K. Kalantar-zadeh, Anodic formation of a thick three-dimensional nanoporous WO_3 film and its photocatalytic property, *Electrochem. Commun.*, 2013, **27**, 128–132.

109 X. Gao, X. Su, C. Yang, F. Xiao, J. Wang, X. Cao, S. Wang and L. Zhang, Hydrothermal synthesis of WO_3 nanoplates as highly sensitive cyclohexene sensor and high-efficiency MB photocatalyst, *Sens. Actuators, B*, 2013, **181**, 537–543.

110 Y. F. Rao, W. Chu and Y. R. Wang, Photocatalytic oxidation of carbamazepine in triclinic-WO_3 suspension: Role of alcohol and sulfate radicals in the degradation pathway, *Appl. Catal., A*, 2013, **468**, 240–249.

111 Y. Lu, G. Liu, J. Zhang, Z. Feng, Z. Li and C. Li, Fabrication of a monoclinic/hexagonal junction in WO_3 and its enhanced photocatalytic degradation of rhodamine B, *Chin. J. Catal.*, 2016, **37**, 349–358.

112 Y. Liu, J. Li, H. Tang, W. Li, Y. Yang, Y. Li and Q. Chen, Enhanced photoelectrochemical performance of plate-like WO_3 induced by surface oxygen vacancies, *Electrochem. Commun.*, 2016, **68**, 81–85.

113 J. Wang, Z. Chen, G. Zhai and Y. Men, Boosting photocatalytic activity of WO_3 nanorods with tailored surface oxygen vacancies for selective alcohol oxidations, *Appl. Surf. Sci.*, 2018, **462**, 760–771.

114 Z. Lou, Q. Gu, L. Xu, Y. Liao and C. Xue, Surfactant-Free Synthesis of Plasmonic Tungsten Oxide Nanowires with Visible-Light-Enhanced Hydrogen Generation from Ammonia Borane, *Chem. – Asian J.*, 2015, **10**, 1291–1294.

115 J. Meng, Q. Lin, T. Chen, X. Wei, J. Li and Z. Zhang, Oxygen vacancy regulation on tungsten oxides with specific exposed facets for enhanced visible-light-driven photocatalytic oxidation, *Nanoscale*, 2018, **10**, 2908–2915.

116 B. Bhuyan, B. Paul, S. S. Dhar and S. Vadivel, Facile hydrothermal synthesis of ultrasmall $W_{18}O_{49}$ nanoparticles and

studies of their photocatalytic activity towards degradation of methylene blue, *Mater. Chem. Phys.*, 2017, **188**, 1–7.

117 X. Zhao, S. Huang, Y. Liu, Q. Liu and Y. Zhang, In situ preparation of highly stable polyaniline/$W_{18}O_{49}$ hybrid nanocomposite as efficient visible light photocatalyst for aqueous Cr(VI) reduction, *J. Hazard. Mater.*, 2018, **353**, 466–475.

118 W. Wei, Y. Yao, Q. Zhao, Z. Xu, Q. Wang, Z. Zhang and Y. Gao, Oxygen defect-induced localized surface plasmon resonance at the WO_{3-x} quantum dot/silver nano-wire interface: SERS and photocatalysis, *Nanoscale*, 2019, **11**, 5535–5547.

119 G. Xi, S. Ouyang, P. Li, J. Ye, Q. Ma, N. Su, H. Bai and C. Wang, Ultrathin $W_{18}O_{49}$ Nanowires with Diameters below 1 nm: Synthesis, Near-Infrared Absorption, Photoluminescence, and Photochemical Reduction of Carbon Dioxide, *Angew. Chem., Int. Ed.*, 2012, **51**, 2395–2399.

120 P. Chen, M. Qin, D. Zhang, Z. Chen, B. Jia, Q. Wan, H. Wu and X. Qu, Combustion synthesis and excellent photocatalytic degradation properties of $W_{18}O_{49}$, *CrystEngComm*, 2015, **17**, 5889–5894.

121 Y. P. Xie, G. Liu, L. Yin and H. Cheng, Crystal facet-dependent photocatalytic oxidation and reduction reactivity of monoclinic WO_3 for solar energy conversion, *J. Mater. Chem.*, 2012, **22**, 6746–6751.

122 D. Zhang, S. Wang, J. Zhu, H. Li and Y. Lu, WO_3 nanocrystals with tunable percentage of (001)-facet exposure, *Appl. Catal., B*, 2012, **123–124**, 398–404.

123 S. Wang, H. Chen, G. Gao, T. Butburee, M. Lyu, S. Thaweesak, J. Yun, A. Du, G. Liu and L. Wang, Synergistic crystal facet engineering and structural control of WO_3 films exhibiting unprecedented photoelectrochemical performance, *Nano Energy*, 2016, **24**, 94–102.

124 Y. Guo, X. Quan, N. Lu, H. Zhao and S. Chen, High Photocatalytic Capability of Self-Assembled Nanoporous WO_3 with Preferential Orientation of (002) Planes, *Environ. Sci. Technol.*, 2007, **41**, 4422–4427.

125 Y. Li, Z. Tang, Z. Zhang and J. Zhang, Enhanced photocatalytic performance of tungsten oxide through tuning exposed facets and introducing oxygen vacancies, *J. Alloys Compd.*, 2017, **708**, 358–366.

126 D. Tanaka, Y. Oaki and H. Imai, Enhanced photocatalytic activity of quantum-confined tungsten trioxide nanoparticles in mesoporous silica, *Chem. Commun.*, 2010, **46**, 5286–5288.

127 A. Fakhri and S. Behrouz, Photocatalytic properties of tungsten trioxide (WO_3) nanoparticles for degradation of Lidocaine under visible and sunlight irradiation, *Sol. Energy*, 2015, **112**, 163–168.

128 S. Shukla, S. Chaudhary, A. Umar, G. R. Chaudhary, S. K. Kansal and S. K. Mehta, Surfactant functionalized tungsten oxide nanoparticles with enhanced photocatalytic activity, *Chem. Eng. J.*, 2016, **288**, 423–431.

129 N. Zhang, C. Chen, Z. Mei, X. Liu, X. Qu, Y. Li, S. Li, W. Qi, Y. Zhang, J. Ye, V. A. L. Roy and R. Ma, Monoclinic Tungsten Oxide with {100} Facet Orientation and Tuned Electronic Band Structure for Enhanced Photocatalytic Oxidations, *ACS Appl. Mater. Interfaces*, 2016, **8**, 10367–10374.

130 C. Sui, J. Gong, T. Cheng, G. Zhou and S. Dong, Fabrication of tungsten oxide microfibers with photocatalytic activity by electrospunning from PVA/$H_3PW_{12}O_{40}$ gel, *Appl. Surf. Sci.*, 2011, **257**, 8600–8604.

131 F. A. Ofori, F. A. Sheikh, R. Appiah-Ntiamoah, X. Yang and H. Kim, A Simple Method of Electrospun Tungsten Trioxide Nanofibers with Enhanced Visible-Light Photocatalytic Activity, *Nano-Micro Lett.*, 2015, **7**, 291–297.

132 H. Zhang, J. Yang, D. Li, W. Guo, Q. Qin, L. Zhu and W. Zheng, Template-free facile preparation of monoclinic WO_3 nanoplates and their high photocatalytic activities, *Appl. Surf. Sci.*, 2014, **305**, 274–280.

133 M. R. Waller, T. K. Townsend, J. Zhao, E. M. Sabio, R. L. Chamousis, N. D. Browning and F. E. Osterloh, Single-Crystal Tungsten Oxide Nanosheets: Photochemical Water Oxidation in the Quantum Confinement Regime, *Chem. Mater.*, 2012, **24**, 698–704.

134 K. Villa, S. Murcia-López, T. Andreu and J. R. Morante, Mesoporous WO_3 photocatalyst for the partial oxidation of methane to methanol using electron scavengers, *Appl. Catal., B*, 2015, **163**, 150–155.

135 A. B. D. Nandiyanto, O. Arutanti, T. Ogi, F. Iskandar, T. O. Kim and K. Okuyama, Synthesis of spherical macroporous WO_3 particles and their high photocatalytic performance, *Chem. Eng. Sci.*, 2013, **101**, 523–532.

136 Z. Chen, J. Wang, G. Zhai, W. An and Y. Men, Hierarchical yolk-shell WO3 microspheres with highly enhanced photoactivity for selective alcohol oxidations, *Appl. Catal., B*, 2017, **218**, 825–832.

137 J. Yu, L. Qi, B. Cheng and X. Zhao, Effect of calcination temperatures on microstructures and photocatalytic activity of tungsten trioxide hollow microspheres, *J. Hazard. Mater.*, 2008, **160**, 621–628.

138 J. Yu, H. Yu, H. Guo, M. Li and S. Mann, Spontaneous Formation of a Tungsten Trioxide Sphere-in-Shell Superstructure by Chemically Induced Self-Transformation, *Small*, 2008, **4**, 87–91.

139 G. Xi, Y. Yan, Q. Ma, J. Li, H. Yang, X. Lu and C. Wang, Synthesis of Multiple-Shell WO_3 Hollow Spheres by a Binary Carbonaceous Template Route and Their Applications in Visible-Light Photocatalysis, *Chem. – Eur. J.*, 2012, **18**, 13949–13953.

140 S. Yao, X. Zhang, F. Qu, A. Umar and X. Wu, Hierarchical WO_3 nanostructures assembled by nanosheets and their applications in wastewater purification, *J. Alloys Compd.*, 2016, **689**, 570–574.

141 S. K. Biswas and J. Baeg, A facile one-step synthesis of single crystalline hierarchical WO_3 with enhanced activity for photoelectrochemical solar water oxidation, *Int. J. Hydrogen Energy*, 2013, **38**, 3177–3188.

142 J. Yu and L. Qi, Template-free fabrication of hierarchically flower-like tungsten trioxide assemblies with enhanced

visible-light-driven photocatalytic activity, *J. Hazard. Mater.*, 2009, **169**, 221–227.

143 Q. Li, L. Wang, D. Chu, X. Yang and Z. Zhang, Cylindrical stacks and flower-like tungsten oxide microstructures: Controllable synthesis and photocatalytic properties, *Ceram. Int.*, 2014, **40**, 4969–4973.

144 R. M. Fernández-Domene, R. Sánchez-Tovar, B. Lucas-Granados, C. S. García-Zamora and J. García-Antón, Customized WO_3 nanoplatelets as visible-light photoelectrocatalyst for the degradation of a recalcitrant model organic compound (methyl orange), *J. Photochem. Photobiol., A*, 2018, **356**, 46–56.

145 M. Sadakane, K. Sasaki, H. Kunioku, B. Ohtani, R. Abe and W. Ueda, Preparation of 3-D ordered macroporous tungsten oxides and nano-crystalline particulate tungsten oxides using a colloidal crystal template method, and their structural characterization and application as photocatalysts under visible light irradiation, *J. Mater. Chem.*, 2010, **20**, 1811–1818.

146 N. Zhang, A. Jalil, D. Wu, S. Chen, Y. Liu, C. Gao, W. Ye, Z. Qi, H. Ju, C. Wang, X. Wu, L. Song, J. Zhu and Y. Xiong, Refining Defect States in $W_{18}O_{49}$ by Mo Doping: A Strategy for Tuning N_2 Activation towards Solar-Driven Nitrogen Fixation, *J. Am. Chem. Soc.*, 2018, **140**, 9434–9443.

147 S. S. Kalanur and H. Seo, Influence of molybdenum doping on the structural, optical and electronic properties of WO_3 for improved solar water splitting, *J. Colloid Interface Sci.*, 2018, **509**, 440–447.

148 S. S. Kalanur and H. Seo, Aligned nanotriangles of tantalum doped tungsten oxide for improved photoelectrochemical water splitting, *J. Alloys Compd.*, 2019, **785**, 1097–1105.

149 W. Mu, X. Xie, X. Li, R. Zhang, Q. Yu, K. Lv, H. Wei and Y. Jian, Characterizations of Nb-doped WO_3 nanomaterials and their enhanced photocatalytic performance, *RSC Adv.*, 2014, **4**, 36064–36070.

150 S. S. Kalanur, I. Yoo and H. Seo, Fundamental investigation of Ti doped WO_3 photoanode and their influence on photoelectrochemical water splitting activity, *Electrochim. Acta*, 2017, **254**, 348–357.

151 F. Mehmood, J. Iqbal, T. Jan, W. Ahmed, W. Ahmed, A. Arshad, Q. Mansoor, S. Z. Ilyas, M. Ismail and I. Ahmad, Effect of Sn doping on the structural, optical, electrical and anticancer properties of WO_3 nanoplates, *Ceram. Int.*, 2016, **42**, 14334–14341.

152 S. S. Kalanur, I. Yoo, K. Eom and H. Seo, Enhancement of photoelectrochemical water splitting response of WO_3 by Means of Bi doping, *J. Catal.*, 2018, **357**, 127–137.

153 F. Mehmood, J. Iqbal, T. Jan and Q. Mansoor, Structural, Raman and photoluminescence properties of Fe doped WO_3 nanoplates with anti cancer and visible light driven photocatalytic activities, *J. Alloys Compd.*, 2017, **728**, 1329–1337.

154 H. Song, Y. Li, Z. Lou, M. Xiao, L. Hu, Z. Ye and L. Zhu, Synthesis of Fe-doped WO_3 nanostructures with high visible-light-driven photocatalytic activities, *Appl. Catal., B*, 2015, **166–167**, 112–120.

155 S. L. Liew, Z. Zhang, T. W. G. Goh, G. S. Subramanian, H. L. D. Seng, T. S. A. Hor, H. K. Luo and D. Z. Chi, Yb-doped WO_3 photocatalysts for water oxidation with visible light, *Int. J. Hydrogen Energy*, 2014, **39**, 4291–4298.

156 L. Xu, D. Gu, X. Chang, L. Chai, Z. Li, X. Jin and S. Sun, Rare-earth-doped tungsten oxide microspheres with highly enhanced photocatalytic activites, *Ceram. Int.*, 2017, **43**, 10263–10269.

157 F. Mehmood, J. Iqbal, T. Jan, A. Gul, Q. Mansoor and R. Faryal, Structural, photoluminescence, electrical, anti cancer and visible light driven photocatalytic characteristics of Co doped WO_3 nanoplates, *Vib. Spectrosc.*, 2017, **93**, 78–89.

158 F. Mehmood, J. Iqbal, A. Gul, W. Ahmed and M. Ismail, Facile synthesis of 2-D Cu doped WO_3 nanoplates with structural, optical and differential anti cancer characteristics, *Physica E*, 2017, **88**, 188–193.

159 X. F. Cheng, W. H. Leng, D. P. Liu, J. Q. Zhang and C. N. Cao, Enhanced photoelectrocatalytic performance of Zn-doped WO_3 photocatalysts for nitrite ions degradation under visible light, *Chemosphere*, 2007, **68**, 1976–1984.

160 F. Mehmood, J. Iqbal, M. Ismail and A. Mehmood, Ni doped WO_3 nanoplates: An excellent photocatalyst and novel nanomaterial for enhanced anticancer activities, *J. Alloys Compd.*, 2018, **746**, 729–738.

161 H. Wang, L. Zhang, K. Wang, X. Sun and W. Wang, Enhanced photocatalytic CO_2 reduction to methane over $WO_3{\cdot}0.33H_2O$ via Mo doping, *Appl. Catal., B*, 2019, **243**, 771–779.

162 J. Kim, C. W. Lee and W. Choi, Platinized WO_3 as an Environmental Photocatalyst that Generates OH Radicals under Visible Light, *Environ. Sci. Technol.*, 2010, **44**, 6849–6854.

163 H. W. Choi, E. J. Kim and S. H. Hahn, Photocatalytic activity of Au-buffered WO_3 thin films prepared by RF magnetron sputtering, *Chem. Eng. J.*, 2010, **161**, 285–288.

164 J. Chen, Y. Ren, T. Hu, T. Xu and Q. Xu, Fabrication and application of substoichiometric tungsten oxide with tunable localized surface plasmon resonances, *Appl. Surf. Sci.*, 2019, **465**, 517–525.

165 S. Sun, W. Wang, S. Zeng, M. Shang and L. Zhang, Preparation of ordered mesoporous Ag/WO_3 and its highly efficient degradation of acetaldehyde under visible-light irradiation, *J. Hazard. Mater.*, 2010, **178**, 427–433.

166 K. A. Willets and R. P. Van Duyne, Localized surface plasmon resonance spectroscopy and sensing, *Annu. Rev. Phys. Chem.*, 2007, **58**, 267–297.

167 W. Hou and S. B. Cronin, A Review of Surface Plasmon Resonance-Enhanced Photocatalysis, *Adv. Funct. Mater.*, 2013, **23**, 1612–1619.

168 Y. Tian and T. Tatsuma, Plasmon-induced photoelectrochemistry at metal nanoparticles supported on nanoporous TiO_2, *Chem. Commun.*, 2004, 1810–1811.

169 J. Ding, L. Zhang, Q. Liu, W. Dai and G. Guan, Synergistic effects of electronic structure of WO_3 nanorods with the dominant {001} exposed facets combined with silver size-dependent on the visible-light photocatalytic activity, *Appl. Catal., B*, 2017, **203**, 335–342.

170 F. Le, D. W. Brandl, Y. A. Urzhumov, H. Wang, J. Kundu, N. J. Halas, J. Aizpurua and P. Nordlander, Metallic Nanoparticle Arrays: A Common Substrate for Both Surface-Enhanced Raman Scattering and Surface-Enhanced Infrared Absorption, *ACS Nano*, 2008, **2**, 707–718.

171 W. Zhu, J. Liu, S. Yu, Y. Zhou and X. Yan, Ag loaded WO_3 nanoplates for efficient photocatalytic degradation of sulfanilamide and their bactericidal effect under visible light irradiation, *J. Hazard. Mater.*, 2016, **318**, 407–416.

172 N. Lu, Z. Zhang, Y. Wang, B. Liu, L. Guo, L. Wang, J. Huang, K. Liu and B. Dong, Direct evidence of IR-driven hot electron transfer in metal-free plasmonic $W_{18}O_{49}$/Carbon heterostructures for enhanced catalytic H_2 production, *Appl. Catal., B*, 2018, **233**, 19–25.

173 T. A. Saleh and V. K. Gupta, Functionalization of tungsten oxide into MWCNT and its application for sunlight-induced degradation of rhodamine B, *J. Colloid Interface Sci.*, 2011, **362**, 337–344.

174 W. Zhu, F. Sun, R. Goei and Y. Zhou, Facile fabrication of RGO-WO_3 composites for effective visible light photocatalytic degradation of sulfamethoxazole, *Appl. Catal., B*, 2017, **207**, 93–102.

175 S. Prabhu, L. Cindrella, O. J. Kwon and K. Mohanraju, Green synthesis of rGO-WO_3 composite and its efficient photoelectrochemical water splitting, *Int. J. Hydrogen Energy*, 2017, **42**, 29791–29796.

176 L. Fu, T. Xia, Y. Zheng, J. Yang, A. Wang and Z. Wang, Preparation of WO_3-reduced graphene oxide nanocomposites with enhanced photocatalytic property, *Ceram. Int.*, 2015, **41**, 5903–5908.

177 X. Li, S. Yang, J. Sun, P. He, X. Xu and G. Ding, Tungsten oxide nanowire-reduced graphene oxide aerogel for high-efficiency visible light photocatalysis, *Carbon*, 2014, **78**, 38–48.

178 H. Khan, M. G. Rigamonti, G. S. Patience and D. C. Boffito, Spray dried TiO_2/WO_3 heterostructure for photocatalytic applications with residual activity in the dark, *Appl. Catal., B*, 2018, **226**, 311–323.

179 M. A. Lara, C. Jaramillo-Páez, J. A. Navío, P. Sánchez-Cid and M. C. Hidalgo, Coupling of WO_3 with anatase TiO_2 sample with high {001} facet exposition: Effect on the photocatalytic properties, *Catal. Today*, 2019, **328**, 142–148.

180 L. Pan, J. Zhang, X. Jia, Y. Ma, X. Zhang, L. Wang and J. Zou, Highly efficient Z-scheme WO_{3-x} quantum dots/TiO_2 for photocatalytic hydrogen generation, *Chin. J. Catal.*, 2017, **38**, 253–259.

181 A. Memar, C. M. Phan and M. O. Tade, Photocatalytic activity of WO_3/Fe_2O_3 nanocomposite photoanode, *Int. J. Hydrogen Energy*, 2015, **40**, 8642–8649.

182 Y. Li, J. Feng, H. Li, X. Wei, R. Wang and A. Zhou, Photoelectrochemical splitting of natural seawater with α-Fe_2O_3/WO_3 nanorod arrays, *Int. J. Hydrogen Energy*, 2016, **41**, 4096–4105.

183 J. Zhang, H. Ma and Z. Liu, Highly efficient photocatalyst based on all oxides WO_3/Cu_2O heterojunction for photoelectrochemical water splitting, *Appl. Catal., B*, 2017, **201**, 84–91.

184 A. K. L. Sajjad, S. Sajjad, A. Iqbal and N. Ryma, ZnO/WO_3 nanostructure as an efficient visible light catalyst, *Ceram. Int.*, 2018, **44**, 9364–9371.

185 Z. Lou, M. Zhu, X. Yang, Y. Zhang, M. Whangbo, B. Li and B. Huang, Continual injection of photoinduced electrons stabilizing surface plasmon resonance of non-elemental-metal plasmonic photocatalyst CdS/WO_{3-x} for efficient hydrogen generation, *Appl. Catal., B*, 2018, **226**, 10–15.

186 L. Zhang, H. Zhang, B. Wang, X. Huang, Y. Ye, R. Lei, W. Feng and P. Liu, A facile method for regulating the charge transfer route of WO_3/CdS in high-efficiency hydrogen production, *Appl. Catal., B*, 2019, **244**, 529–535.

187 C. Liu, Y. Yang, W. Li, J. Li, Y. Li and Q. Chen, Construction of novel Bi_2S_3 nanobelt @ WO_3 nanoplate arrays on FTO glass with high photoelectrochemical activity, *Int. J. Hydrogen Energy*, 2016, **41**, 5878–5886.

188 J. Rong, T. Zhang, F. Qiu, X. Rong, X. Zhu and X. Zhang, Preparation of hierarchical micro/nanostructured Bi_2S_3-WO_3 composites for enhanced photocatalytic performance, *J. Alloys Compd.*, 2016, **685**, 812–819.

189 L. Ye and Z. Wen, $ZnIn_2S_4$ nanosheets decorating WO_3 nanorods core-shell hybrids for boosting visible-light photocatalysis hydrogen generation, *Int. J. Hydrogen Energy*, 2019, **44**, 3751–3759.

190 T. Wang, W. Quan, D. Jiang, L. Chen, D. Li, S. Meng and M. Chen, Synthesis of redox-mediator-free direct Z-scheme AgI/WO_3 nanocomposite photocatalysts for the degradation of tetracycline with enhanced photocatalytic activity, *Chem. Eng. J.*, 2016, **300**, 280–290.

191 Y. L. Qi, Y. F. Zheng and X. C. Song, Synthesis and enhanced visible light photocatalytic activity of WO_3-$BiOCl_xBr_{1-x}$ heterojunctions with tunable energy band structure, *Ceram. Int.*, 2017, **43**, 12302–12310.

192 E. Grilla, A. Petala, Z. Frontistis, I. K. Konstantinou, D. I. Kondarides and D. Mantzavinos, Solar photocatalytic abatement of sulfamethoxazole over Ag_3PO_4/WO_3 composites, *Appl. Catal., B*, 2018, **231**, 73–81.

193 S. Xu, D. Fu, K. Song, L. Wang, Z. Yang, W. Yang and H. Hou, One-dimensional WO_3/$BiVO_4$ heterojunction photoanodes for efficient photoelectrochemical water splitting, *Chem. Eng. J.*, 2018, **349**, 368–375.

194 Y. Liu, B. R. Wygant, K. Kawashima, O. Mabayoje, T. E. Hong, S. Lee, J. Lin, J. Kim, K. Yubuta, W. Li, J. Li and C. B. Mullins, Facet effect on the photoelectrochemical performance of a WO_3/$BiVO_4$ heterojunction photoanode, *Appl. Catal., B*, 2019, **245**, 227–239.

195 J. Zhu, W. Li, J. Li, Y. Li, H. Hu and Y. Yang, Photoelectrochemical activity of $NiWO_4$/WO_3 heterojunc-

tion photoanode under visible light irradiation, *Electrochim. Acta*, 2013, **112**, 191–198.

196 M. Gui, W. Zhang, Y. Chang and Y. Yu, One-step hydrothermal preparation strategy for nanostructured WO_3/Bi_2WO_6 heterojunction with high visible light photocatalytic activity, *Chem. Eng. J.*, 2012, **197**, 283–288.

197 Y. Peng, Q. Chen, D. Wang, H. Zhou and A. Xu, Synthesis of one-dimensional WO_3-Bi_2WO_6 heterojunctions with enhanced photocatalytic activity, *CrystEngComm*, 2015, **17**, 569–576.

198 Y. Xiao, X. Tao, G. Qiu, Z. Dai, P. Gao and B. Li, Optimal synthesis of a direct Z-scheme photocatalyst with ultrathin $W_{18}O_{49}$ nanowires on g-C_3N_4 nanosheets for solar-driven oxidation reactions, *J. Colloid Interface Sci.*, 2019, **550**, 99–109.

199 J. Chen, X. Xiao, Y. Wang and Z. Ye, Fabrication of hierarchical sheet-on-sheet WO_3/g-C_3N_4 composites with enhanced photocatalytic activity, *J. Alloys Compd.*, 2019, **777**, 325–334.

200 Z. Huang, J. Song, X. Wang, L. Pan, K. Li, X. Zhang, L. Wang and J. Zou, Switching charge transfer of C_3N_4/$W_{18}O_{49}$ from type-II to Z-scheme by interfacial band bending for highly efficient photocatalytic hydrogen evolution, *Nano Energy*, 2017, **40**, 308–316.

201 H. Xu, H. Zhao, Y. Xu, Z. Chen, L. Huang, Y. Li, Y. Song, Q. Zhang and H. Li, Three-dimensionally ordered macroporous WO_3 modified Ag_3PO_4 with enhanced visible light photocatalytic performance, *Ceram. Int.*, 2016, **42**, 1392–1398.

202 H. Zhou, Z. Wen, J. Liu, J. Ke, X. Duan and S. Wang, Z-scheme plasmonic Ag decorated WO_3/Bi_2WO_6 hybrids for enhanced photocatalytic abatement of chlorinated-VOCs under solar light irradiation, *Appl. Catal., B*, 2019, **242**, 76–84.

